Nano Research

ISSN 1998-0124 CN 11-5974/O4
https://doi.org/10.26599/NR.2026.94908539

Research Article

An injectable AsCu-nanocomposite hydrogel breaks the pathological triad of acute osteomyelitis via synergistic bactericidal and macrophage-reprogramming therapy

Vidmi Taolam Martin[1,2,§], Yanpeng Lin[3,§], Hangtian Wu[1,2,§], Bo Yu[4], Daogang Guan[5,6](✉), Jun Wang[7](✉), Bin Yu[1,2](✉)

[1] Division of Orthopaedics and Traumatology, Department of Orthopaedics, Nanfang Hospital, Southern Medical University, Guangzhou 510515, China

[2] Guangdong Provincial Key Laboratory of Bone and Cartilage Regeneration Medicine, Nanfang Hospital, Southern Medical University, Guangzhou 510515, China

[3] Department of Radiology, Nanfang Hospital, Southern Medical University, Guangzhou 510515, China

[4] Department of Orthopaedics and Traumatology, Zhujiang Hospital, Southern Medical University, Guangzhou 510282, China

[5] Department of Biochemistry and Molecular Biology, School of Basic Medical Sciences, Southern Medical University, Guangzhou 510515, China

[6] Guangdong Provincial Key Laboratory of Single Cell Technology and Application, Southern Medical University, Guangzhou 510515, China

[7] School of Animal Science and Technology, Foshan University, Foshan 528231, China

[§] Vidmi Taolam Martin, Yanpeng Lin, and Hangtian Wu contributed equally to this work.

Nano Res., **Just Accepted Manuscript** • https://doi.org/10.26599/NR.2026.94908539

https://www.sciopen.com/journal/1998-0124 on Feb. 4, 2026

TABLE OF CONTENTS (TOC)

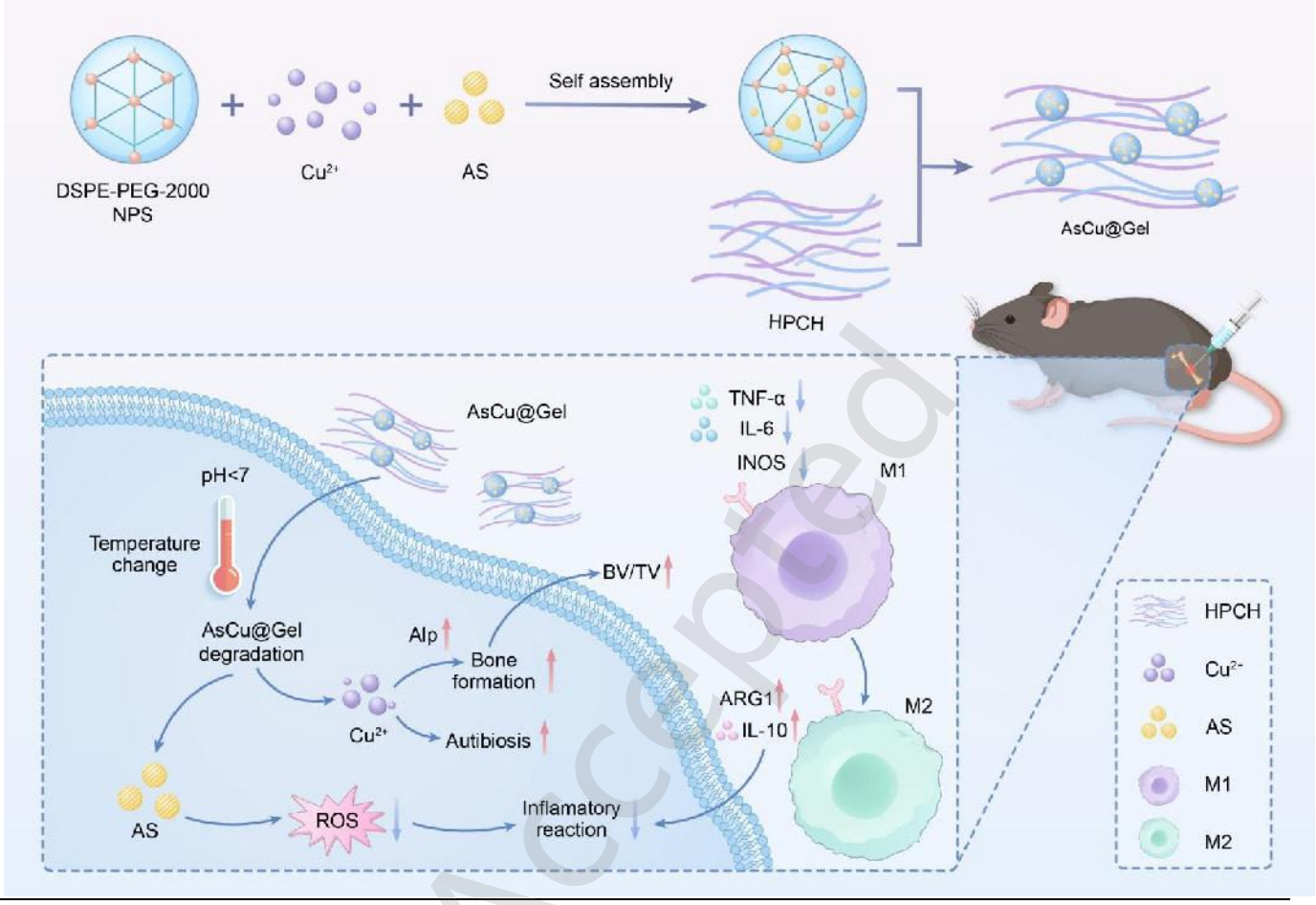

An injectable AsCu-nanocomposite hydrogel addresses the pathological triad of acute osteomyelitis by simultaneously eradicating biofilms, inducing macrophage polarization from the M1 to M2 phenotype, and facilitating functional bone regeneration.

Nano Research

Open Access

Research Article

An injectable AsCu-nanocomposite hydrogel breaks the pathological triad of acute osteomyelitis via synergistic bactericidal and macrophage-reprogramming therapy

Vidmi Taolam Martin[1,2,§], Yanpeng Lin[3,§], Hangtian Wu[1,2,§], Bo Yu[4], Daogang Guan[5,6*] ✉, Jun Wang[7*] ✉, and Bin Yu[1,2*] ✉

[1] *Division of Orthopaedics and Traumatology, Department of Orthopaedics, Nanfang Hospital, Southern Medical University, Guangzhou 510515, China*
[2] *Guangdong Provincial Key Laboratory of Bone and Cartilage Regeneration Medicine, Nanfang Hospital, Southern Medical University, Guangzhou 510515, China*
[3] *Department of Radiology, Nanfang Hospital, Southern Medical University, Guangzhou 510515, China*
[4] *Department of Orthopaedics and Traumatology, Zhujiang Hospital, Southern Medical University, Guangzhou 510282, China*
[5] *Department of Biochemistry and Molecular Biology, School of Basic Medical Sciences, Southern Medical University, Guangzhou 510515, China*
[6] *Guangdong Provincial Key Laboratory of Single Cell Technology and Application, Southern Medical University, Guangzhou 510515, China*
[7] *School of Animal Science and Technology, Foshan University, Foshan 528231, China*
[§] *Vidmi Taolam Martin, Yanpeng Lin, and Hangtian Wu contributed equally to this work.*

Received: 3 December 2025; **Revised:** 4 February 2026; **Accepted:** 4 February 2026

✉ Address correspondence to Daogang Guan, guandg0929@smu.edu.cn; Jun Wang, wangjun@fosu.edu.cn; Bin Yu, yubin@smu.edu.cn

Cite this article: *Nano Research*, **2026**, *19*, 94908539. https://doi.org/10.26599/NR.2026.94908539

ABSTRACT: The clinical failure of conventional osteomyelitis treatments often arises from their inability to concurrently eradicate biofilms, resolve chronic inflammation, and promote bone repair. Therefore, there is an urgent need for a therapeutic approach that simultaneously addresses infection, immune dysregulation, and tissue loss. This study aims to develop a multifunctional nanocomposite hydrogel (AsCu@Gel) that integrates antibacterial, immunomodulatory, and osteoinductive properties for the comprehensive treatment of acute *Staphylococcal* osteomyelitis (AOM). We engineered a thermosensitive hydrogel encapsulating Astaxanthin-Copper nanoparticles (AsCu@NPs). The material was characterized for its structure, multi-stimuli responsive release (pH, enzyme, temperature), and biocompatibility. Its efficacy was evaluated through *in vitro* antibacterial and anti-biofilm assays, analysis of macrophage polarization, and osteogenic differentiation studies. A mouse model of implant-associated AOM was used to validate the *in vivo* therapeutic effects, immune modulation, and bone preservation. The AsCu@Gel system demonstrated potent, pH-enhanced antibacterial and anti-biofilm activity. Crucially, it synergistically polarized macrophages from a pro-inflammatory M1 to a pro-healing M2 phenotype, significantly elevating IL-10, ARG1, and CD206 while suppressing TNF-α, IL-6, and iNOS. Network pharmacology and experimental validation revealed that this dual action downregulated key inflammatory pathways (e.g., TLR9, MAPK8) and upregulated osteogenic signals (e.g., AKT1). *In vivo*, AsCu@Gel effectively eradicated infection, resolved systemic and local inflammation, and preserved bone architecture, outperforming monotherapy controls. The AsCu@Gel platform represents a shift from simple antibacterial treatment to a comprehensive strategy of anti-infection, anti-inflammatory, and pro-regeneration. Simultaneously disrupting biofilms and reprogramming the immune microenvironment toward regeneration offers a promising and innovative solution for treating complex bone infections.

KEYWORDS: osteomyelitis, nanocomposite hydrogel, macrophage polarization, immunomodulation, bone regeneration

Introduction

The clinical management of acute *Staphylococcal* osteomyelitis (AOM) represents a significant biomedical challenge, primarily due to its progression into a chronic, self-sustaining condition. This pathological triad is characterized by resilient bacterial biofilms, a dysregulated M1 macrophage-dominated inflammatory response that leads to tissue destruction, and a subsequent failure of regenerative processes [1-3]. Conventional treatments, such as systemic antibiotics and non-degradable poly(methyl methacrylate) (PMMA) beads, continue to be the standard of care; however, they are fundamentally inadequate. These methods serve only as passive drug depots and lack the dynamic immunomodulatory and osteogenic functions required to break the disease cycle and prevent chronic conditions [4-6]. Therefore, there is a critical unmet need for advanced strategies capable of simultaneously dismantling biofilms, resolving inflammation, and actively promoting bone regeneration.

Copper ions (Cu^{2+}) represent a promising therapeutic foundation due to their broad-spectrum antibacterial activity and well-documented capacity to promote angiogenesis and osteogenesis [7, 8]. However, the translational potential of current Cu^{2+} delivery systems is limited. Their reliance on single-stimulus release mechanisms often results in inadequate spatiotemporal control and potential cytotoxicity from burst

release [8-10]. More critically, a predominant limitation of these systems is their neglect of the host immune response. Persistent M1-dominated inflammation, even after partial bacterial eradication, directly impedes bone healing and ultimately constrains the therapeutic efficacy of purely antibacterial materials [11-13].

To overcome these intertwined challenges, we hypothesized that overcoming AOM requires a single, integrated platform capable of coordinated action against all three pathological pillars. Accordingly, we developed AsCu@Gel, an injectable and biodegradable nanocomposite hydrogel designed for orchestrated triple-therapy. This system utilizes a dual-responsive hydroxypropyl chitin matrix for targeted co-delivery [14, 15], employing DSPE-PEG_{2000} to encapsulate a novel nano-formulation of astaxanthin (*As*) and Cu^{2+}, thereby enhancing stability and enabling controlled release.

The platform's innovation is rooted in a multi-functional design that actively intervenes at multiple disease stages: First, it features spatiotemporally controlled release, responding to temperature for injectability and to the acidic biofilm microenvironment, ensuring precise therapeutic deployment [16-18]. Second, it provides synergistic antibacterial action, where localized, potent bactericidal activity from Cu^{2+} works to eradicate established biofilms [19, 20]. Third, and most significantly, it enables active immunomodulation, wherein *As* scavenges reactive oxygen species (ROS) and, in synergy with Cu^{2+}, reprograms macrophages from a destructive M1 to a regenerative M2 phenotype [21-23]. Finally, this resolved, pro-healing microenvironment permits robust osteogenic activation, driven by the controlled release of Cu^{2+}[24].

Unlike previous approaches that simply combine functions [25-29], AsCu@Gel is designed from the ground up to break the pathological feedback loops of AOM. We demonstrate that this integrated platform not only eradicates biofilms but also mechanistically reprograms the host immune response, thereby breaking the cycle of chronic inflammation and creating the conditions for robust bone regeneration. This work establishes a new therapeutic paradigm in which advanced material design is leveraged to orchestrate a comprehensive healing process for complex infectious diseases.

2.Results and Discussion

2.1 Synthesis and characterization of AsCu@DSPE-PEG_{2000} nanoparticles and gel composite

The Astaxanthin-copper nanoparticles (AsCu@DSPE-PEG_{2000}) were successfully synthesized via a co-assembly method, with DSPE-PEG_{2000} providing colloidal stability **(Table S1)**. Transmission electron microscope (TEM) **(Figure 1A)** and dynamic light scattering (DLS) **(Figure 1B)** revealed monodisperse spherical nanoparticles (10-100 nm; PDI < 0.2), enabling bone marrow penetration [30], optimally sized for targeting early osteomyelitis lesions through (1) enhanced vascular permeability during acute inflammation, and (2) preferential accumulation in newly formed porous bone structures characteristic of early-stage infection. Thermogravimetric (TGA) analysis demonstrated exceptional thermal stability up to 176°C, with 22.56% residual Cu^{2+} content, suggesting robust inorganic-organic hybrid architecture **(Figure 1C)**. X-ray photoelectron spectroscopy (XPS) spectra confirmed Cu^{2+} coordination (Cu2p3/2 at 932.5 eV with satellite peaks) and retention of DSPE-PEG_{2000}'s molecular integrity (C1s, O1s, P2p peaks) **(Table S2)**, critical for *in vivo* stealth properties **(Figure 1D–H)** [31, 32]. The release kinetics are consistent with the intended strategy for deep tissue targeting and microenvironment compatibility. The initial burst release (**Figure 1I**, 40% in 6 h) at pH 5.0 produces a high local drug concentration, which penetrates and disrupts the dense extracellular matrix of biofilms, thereby enabling deep tissue targeting. Subsequently, a sustained release phase (80% over 72 h) maintains therapeutic drug levels to resolve inflammation and protect surrounding osteoblasts from cytotoxic damage. This approach supports microenvironment compatibility and facilitates bone repair, as demonstrated by enhanced alkaline phosphatase (ALP) activity [33-35]. Time-course quantification (DiI, R^2>0.99, **Figure 1J**) showed maximal nanoparticle accumulation during the critical 24-72h therapeutic window for early osteomyelitis (3.8× vs. healthy bone), correlating with peak inflammatory marker expression [36]. However, hydrogel formulations (As@Gel, Cu@Gel, AsCu@Gel) exhibited thermoresponsive behavior **(Table S3)**, maintaining injectability at 4°C while forming stable depots at 37°C **(Figure 1K and L)**. This multifunctional platform addresses the dual challenges of biofilm eradication and bone regeneration through (a) pH-activated Cu^{2+} release in acidic infection microenvironments, (b) ROS-scavenging *As* protection, and (c) localized hydrogel delivery minimizing systemic exposure [37, 38].

Rheological analysis demonstrated the thermoresponsive and mechanically robust properties of the AsCu@Gel composite (**Figure S1**). The composite underwent a pronounced sol-gel transition near 16-17 °C, with the storage modulus (G′) increasing by more than three orders of magnitude to exceed 80 Pa at 37 °C. This result indicates the formation of a stable, elastic network at physiological temperature. Frequency sweeps revealed solid-like behavior (G′ > G″ across 0.6-600 rad/s) and shear-thinning viscosity, supporting both the injectability and mechanical stability required for an in-situ forming bone defect filler.

Further analysis indicated that the *in vitro* release kinetics of Cu^{2+} from the AsCu@Gel composite (**Figure S2**) exhibited a multi-stimuli-responsive profile, with the release critically dependent on pH, temperature, and hyaluronidase. Among these factors, pH was identified as the primary determinant of release kinetics, aligning with established design principles for smart hydrogels [39].

After 72 h, the cumulative release was significantly higher at pH 6.5 (45.3 ± 1.3%) compared to physiological pH 7.4 (24.0 ± 0.8%; p < 0.0001, unpaired t-test). The observed pH-dependent release can be attributed to the protonation of amine groups in the hydrogel matrix, which increases electrostatic repulsion and swelling in acidic environments. This mechanism, well-documented for polysaccharide-based hydrogels [40], reduces the mesh size of the polymer network, enhancing the diffusion of encapsulated AsCu@NPs). The resulting changes facilitate ion exchange between Cu^{2+} and protons (H^+) [41], supporting targeted and controlled release in acidic microenvironments.

Additionally, a consistent thermoresponsive release profile was observed. Under identical pH conditions, increasing the temperature from 37°C to 40°C resulted in a modest but statistically significant increase in Cu^{2+} release at pH 7.4 (26.0 ± 1.0% compared to 24.0 ± 0.8%; p < 0.05). This accelerated release at mildly hyperthermic temperatures is characteristic of hydrogel-based delivery systems and is attributed to increased polymer chain mobility and enhanced diffusion rates [42]. These findings suggest that mild hyperthermia may improve therapeutic availability.

The release system also demonstrated a strong enzymatic bio-response. The addition of hyaluronidase, an enzyme upregulated at infection and inflammation sites [42], significantly increased Cu^{2+} release under all tested conditions. This effect is explained by the enzymatic degradation of glycosidic bonds within the polysaccharide network, which increases matrix porosity and creates additional diffusion pathways [44]. Thus, enzymatic responsiveness provides a bio-functional mechanism for spatiotemporal release in response to pathological stimuli.

The combined action of these stimuli enables the controlled

release of a therapeutically effective dose of Cu^{2+} at the infection site, surpassing the minimum bactericidal concentration required for treating *S. aureus* biofilms. Simultaneously, this system minimises premature release, reducing potential toxicity to surrounding healthy tissues, which is a primary objective of targeted antimicrobial delivery systems [45].

Further, The *in vitro* degradation and release kinetics of the AsCu@Gel system were systematically evaluated over 72 h (**Figure S3A–C**). The hydrogel demonstrated a characteristic pH-responsive swelling and erosion behavior, consistent with the dual-sensitive properties of the hydroxypropyl chitin (HPCH) matrix [46, 47]. The medium pH decreased from physiological levels (approximately 7.8) to a stable acidic plateau (approximately 5.0) within 24 h, likely reflecting initial ion exchange (Cu^{2+}/H^{+}) and activation of the pH-responsive swelling of the HPCH network (**Figure S3A**). Simultaneously, the hydrogel mass loss plateaued at approximately 9.5%, indicating that the crosslinked gel network remained largely intact with over 90% mass retention (**Figure S3B**). These results demonstrate the structural stability of the nanocomposite hydrogel, suggesting its suitability for extended *in vivo* residence. Cumulative Cu^{2+} release exhibited a triphasic profile: an initial burst release (approximately 10% within 2 h, attributed to surface-associated ions), a sustained release phase (up to approximately 85% at 24 h), and a final plateau approaching 90% by 72 h. The sustained release phase closely correlated with the period of most rapid pH decrease and mass loss, supporting a release mechanism driven by pH-triggered gel swelling [48, 49]. This process increases mesh size and facilitates the diffusion of encapsulated AsCu nanoparticles, followed by gradual nanoparticle dissociation (**Figure S3C**).

In summary, the AsCu@Gel system does not undergo conventional bulk erosion. Instead, it exhibits a predictable, swelling-controlled release of nanoparticle payloads while maintaining a stable crosslinked scaffold. This multi-stage release mechanism, which combines pH-responsive matrix swelling, nanoparticle diffusion, and subsequent nanoparticle dissociation, ensures sustained and coordinated delivery of both *As* and Cu^{2+}. Therefore, the AsCu@Gel system represents a promising platform for targeted combination therapy.

2.2 AsCu@Gel eradicates *S. aureus* through synergistic bactericidal activity and biofilm suppression *in vitro*

The viability of *S. aureus* significantly decreased to approximately 51.46% following treatment with AsCu@Gel, highlighting its strong antibacterial efficacy **(Figure 2A and B)**. To further investigate the effects of AsCu@Gel on *S. aureus* proliferation, we monitored the OD_{600} of the *S. aureus* suspension on days 1, 3, and 7. Notably, AsCu@Gel consistently inhibited *S. aureus* growth throughout these 7 days **(Figure 2C)**. Analysis of colony formation revealed a significant reduction in *S. aureus* counts at both days 3 and 7 following treatment with AsCu@Gel compared to the control group **(Figure 2D)**. We also assessed the impact of AsCu@Gel on the formation of *S. aureus* biofilms by co-culturing the bacteria with the test materials for 24 h. Crystal violet staining demonstrated that AsCu@Gel significantly reduced biofilm formation, as confirmed by the crystal violet eluent's optical density (OD_{590}) **(Figure 2E and F)**. To further validate the bacteriostatic effect of the material, we quantified the sizes of the inhibition zones. Our results indicated that the bacteriostatic area associated with the AsCu@Gel group was considerably larger than that of the Cu@Gel group **(Figure 2G and H)**. This indicates that AsCu@Gel has significant antibacterial effects, probably due to the sustained release of antibiotics from the material . In summary, these results show that AsCu@Gel effectively inhibits both bacterial growth and biofilm formation *in vitro*.

The antibacterial properties of the hydrogels were systematically assessed by monitoring bacterial growth kinetics using OD_{600} measurements after 24 h of incubation (**Figure S4A and S4B**). The plain HPCH hydrogel (Gel) exhibited OD_{600} values of 0.949–0.961, which were comparable to the positive control (**Figure 2G and 2H**), confirming the biocompatible and non-antibacterial characteristics of the polysaccharide matrix. This outcome excludes the hydrogel carrier as a source of antimicrobial interference. In contrast, the Cu-loaded hydrogel (Cu@Gel) demonstrated significant antibacterial activity, reducing OD_{600} to 0.223–0.228 (approximately 76% inhibition compared to Gel; $p<0.001$). This inhibition is consistent with the established biocidal properties of Cu^{2+} ions, which induce oxidative stress, protein dysfunction, and membrane damage in bacterial cells. The As-Cu composite hydrogel (AsCu@Gel) achieved the highest level of inhibition, lowering OD_{600} to 0.158–0.162 (approximately 83% inhibition), which was statistically superior to the Cu group. Although the As-only hydrogel (As@Gel) exhibited limited antibacterial activity (OD_{600} = 0.89), its combination with Cu significantly enhanced the overall bactericidal effect. This observation suggests a synergistic or additive interaction between As and Cu, potentially through accelerated ion release, increased bacterial membrane permeability, or enhanced intracellular accumulation of Cu^{2+}.

To investigate the antimicrobial mechanism, SYTOX-Green membrane integrity assays were conducted. As shown in **Figure S4C**, strong green fluorescence was observed in bacteria treated with Cu and AsCu hydrogels, indicating substantial nucleic acid leakage resulting from loss of membrane integrity. This visual evidence supports the OD_{600} data and indicates a membrane-disruption-mediated killing mechanism for Cu^{2+}. Although ultrastructural imaging (SEM/TEM) and metabolic profiling (ATP assays) would provide further mechanistic insights, the combined growth inhibition, membrane leakage, and ion release data collectively demonstrate that: (1) Cu^{2+} is the primary antibacterial agent in the nanocomposite hydrogel; (2) As enhances the efficacy of Cu^{2+}, likely by modifying its bioavailability or interaction with bacterial membranes; and (3) the HPCH matrix is inert and does not contribute to antibacterial activity. These results highlight the potential of As-Cu nanocomposite hydrogels as a promising platform for localized antibacterial applications, where the synergistic use of metal ions can enhance efficacy while minimizing the individual doses of each ion.

2.3 AsCu@Gel exhibits excellent cytocompatibility and hemocompatibility while maintaining anti-inflammatory properties

To verify the biocompatibility of AsCu@Gel as an implantable lubricating biomaterial, we assessed its cytotoxicity and cytocompatibility *in vitro* using chondrocytes. CCK8 assays determined that the optimal dosage of AsCu@Gel within the hydrogel was 10 μg/mL after 24 h of culture **(Figure 3A)**. Live/dead staining **(Figure 3B)** and quantitative analysis **(Figure 3D)** indicated that the viability of RAW264.7 cells across all nanocomposite hydrogel groups remained above 95% after 24-h incubation, with no significant differences observed between the groups. This finding underscores the exceptional cytocompatibility of the nanocomposite hydrogel. Furthermore, cytoskeleton staining results showed no noticeable changes in cell morphology for RAW264.7 lines when exposed to the various nanocomposite hydrogel compared to the control group **(Figure 3C)**. Notably, all nanocomposite hydrogel demonstrated hemolysis ratios below 2%, which is considerably lower than the critical safe hemolysis ratio of 5% established for biomaterials according to the ASTM standard (F756-2008) **(Figure 3E)** [51, 52]. This further highlights the outstanding cytocompatibility of the nanocomposite hydrogel.

2.4 Network pharmacology elucidates the multi-target

therapeutic efficacy of *As* in the treatment of acute *Staphylococcal* osteomyelitis

To explore the underlying mechanisms of *As* treatment in AOM, the 2D molecular structure of *As* was obtained from the PubChem database, and 100 pharmacological targets were predicted using the SwissTargetPrediction database **(Figure 4A)**. Next, the intersecting genes of *As* and AOM (13 genes) were identified **(Figure 4B)**. The most significant modules were extracted from a PPI network by using MCODE. Ten core gene targets were identified using CytoHubba, including IDO1, FLT3, TERT, TLR9, SRC, MAPK8, NOS2, MMP9, AKT1, and CSF1R; G6PD is also present but not in the MCC top 10, suggesting it may be less central in this context **(Figure 4C and D)**. The results of the gene analysis suggest that *As* may have an impact on various cellular processes, such as response to molecules of bacterial origin (TLR9 and NOS2), cellular response to oxidative stress (NOS2 and AKT1), regulation of protein serine/threonine kinase activity (AKT1 and MAPK8), osteoclast-related terms (e.g., mammary gland development shares pathways with bone remodeling, CSF1R and SRC), transmembrane receptor protein tyrosine kinase activity (FLT3 and CSF1R), and heme binding/NADP binding (IDO1 and NOS2) **(Figure 4E)**. KEGG analysis revealed 30 significantly enriched pathways (*p*-adjusted threshold of <0.05), with predominant involvement of osteoclast differentiation, pathogen-host interaction (e.g., Toll-like receptor signaling), and oxidative stress pathways **(Figure 4F)** [53-55]. These align with *As*'s dual role in mitigating bacterial infection and preserving bone homeostasis [21].

2.5 AsCu@Gel polarizes macrophages toward anti-inflammatory M2 phenotype and mitigates LPS-induced inflammation

Macrophages are central to the immune response in osteomyelitis, but their dysregulation can contribute to chronic infection and bone damage. Understanding the role of macrophages is crucial for developing effective treatments. Targeting macrophage polarization, such as promoting M1 for bacterial killing or M2 for tissue repair, represents a potential therapeutic strategy [56]. Bacterial components (e.g., lipopolysaccharide (LPS) from Gram-negative bacteria) are the main features that contribute to the activation of macrophages [57]. We exposed LPS-stimulated RAW264.7 cells to different nanocomposite hydrogel to address this query. Our goal was to assess if AsCu@Gel could mitigate the features of proinflammatory cytokines under *in vitro* conditions. In our study, we utilized an Edu staining **(Figure 5A and D)** to assess the proliferation of RAW264.7 cells when treated with various nanocomposite hydrogel groups. After LPS activation, AsCu@Gel effectively inhibited the proliferation of RAW 264.7 cells. These results demonstrate that AsCu@Gel can attenuate the proliferation and migration of activated macrophages.

As mentioned in the literature, oxidative stress and chronic inflammation are central to osteomyelitis, causing bone damage and inhibiting healing [58]. We further assessed the antioxidative effects of AsCu@Gel on RAW264.7 cells by evaluating its efficacy in scavenging ROS using DCFH-DA as a probe. LPS was incubated with RAW264.7 cells to induce oxidative stress. The green fluorescence signaling in different treated cells was detected by a fluorescence microscope and depicted in **Figure 5B and E**. A noticeable increase in ROS signal was observed in the LPS-treated group, indicating that LPS successfully induced cellular oxidative stress. In contrast, treatment with AsCu@Gel led to a significant reduction in the fluorescence, providing strong evidence for their ability to mitigate intracellular ROS production and exhibit potent antioxidative properties effectively.

To further investigate the impact of AsCu@Gel on the anti-inflammatory effect of RAW264.7 cells. We analyzed the apoptosis of macrophage cells in each treatment group by flow cytometry. Our findings revealed that the anti-inflammatory effect of the nanoparticles hydrogel did not stem from an increase in macrophage apoptosis **(Figure 5C and F)**. Macrophages are essential for regulating inflammation through two main types: M1 and M2. M1 macrophages are crucial for fighting infection in the early stages of osteomyelitis. However, if this response is not properly managed or shifts to M2, it can lead to chronic inflammation, bone destruction, and impaired bone regeneration. This has prompted us to investigate whether AsCu@Gel can regulate macrophage polarization. In the early stages of osteomyelitis, Inducible Nitric Oxide Synthase (iNOS) is upregulated by lipoteichoic acid (LTA) and various bacterial components [59]. Although iNOS is important for controlling infection, it can also worsen inflammation and contribute to bone damage. Inhibiting iNOS may reduce the excessive production of nitric oxide (NO) and mitigate inflammation, thus helping to protect the bones.

The TNF-α and IL-6 cytokine profile, coupled with high iNOS-derived nitric oxide (NO) production from LPS-activated M1 macrophages, creates a highly inflammatory microenvironment that stimulates osteoclastogenesis, leading to the degradation of the bone matrix and clinical bone deterioration [60, 61]. The LPS-treated group exhibited a significant upregulation of these pro-inflammatory cytokines, suggesting an M1 state in macrophages. Our findings highlight a key limitation of single-agent therapies for osteomyelitis. The Cu@Gel group showed strong antibacterial effects but did not fully resolve inflammation, as indicated by only partial reductions in M1 markers (iNOS, IL-6, TNF-α; **Figure 5G–I**) [62]. This supports existing evidence that metal-ion therapies can control infection but often leave a lingering pro-inflammatory state that hinders tissue repair [63, 64]. In contrast, As@Gel reduced inflammation but did not promote regeneration, demonstrating that anti-inflammatory effects alone are insufficient. Only the combined AsCu@Gel treatment achieved comprehensive immune modulation. *As* suppressed the M1 response, while Cu^{2+} promoted the pro-healing M2 phenotype, significantly increasing ARG1, CD206, and IL-10 expression (**Figure 5J-L**) [65]. This dual action led to a marked shift in macrophage polarization, as shown by higher ARG1/iNOS and CD206/TNF-α ratios (**Figure 5M, N**) and increased IL-10/TNF-α and IL-10/IL-6 ratios (**Figure S5**). As a result, AsCu@Gel not only suppresses harmful inflammation but also initiates tissue regeneration, breaking the cycle of chronic inflammation and supporting bone healing.

To validate pathological relevance, we compared AsCu@Gel's effects under LPS (**Figure 5A, 5I, 5J, 5L, 5M, and S5A**) versus LTA (**Figure S6A–H**) stimulation. As expected, LTA induced a moderated pro-inflammatory state compared to the potent TLR4 agonist LPS, consistent with distinct signaling pathways (TLR2 vs. TLR4) [66, 67]. AsCu@Gel remained highly effective under LTA, suppressing M1 markers (**Figure S6A and S6B**) while enhancing M2 markers (**Figure S6C and S6D**). Strikingly, the ARG1/iNOS polarization ratio, a key metric of macrophage fate [68], increased significantly more with LTA than with LPS (1.9-fold, $p = 0.0486$; **Figure S6G**). A similar trend was observed for IL-10/TNF-α (1.5-fold, $p = 0.0925$; **Figure S6H**). This demonstrates that AsCu@Gel's macrophage-reprogramming action is enhanced in the Gram-positive context, indicating a pathogen-optimized mechanism that aligns with the TLR2-dominated signaling known to drive chronic inflammation and bone destruction in *Staphylococcal* osteomyelitis [69, 70].

2.6 Protein-level validation reveals coordinated signaling reprogramming by AsCu@Gel

To mechanistically validate the network pharmacology predictions at the protein level, Western blot analysis was conducted for total and phosphorylated forms of key targets (TLR9, MAPK8, and AKT1). Total protein analysis demonstrated

that AsCu@Gel significantly upregulated AKT1 expression compared to LPS-stimulated controls (1.41-fold, $p < 0.01$), while differentially modulating TLR9 and MAPK8 levels (**Figure S7A–D**). Phosphorylation analysis further revealed a distinct signaling reprogramming pattern, AsCu@Gel treatment suppressed activation of pro-inflammatory pathways, as indicated by reduced phosphorylation of both TLR9 and MAPK8, while maintaining strong activation of the pro-regenerative AKT1 pathway (p-AKT1) (**Figure S7A&D**). This coordinated modulation provides direct protein-level mechanistic insight into the immunomodulatory action of AsCu@Gel. Suppression of p-TLR9 and p-MAPK8 corresponds with downregulation of M1 inflammatory markers, thereby reducing drivers of tissue-destructive inflammation. Simultaneously, sustained activation of p-AKT1 signals enhanced cell survival, M2 polarization, and osteogenic differentiation. This dual-pathway intervention, which inhibits inflammatory signaling while activating reparative pathways, accounts for the efficacy of AsCu@Gel in disrupting the self-perpetuating cycle of infection and inflammation in osteomyelitis. These findings suggest that the platform extends beyond passive antibacterial delivery to actively reconfigure the host's intracellular signaling environment, thereby transforming a pathological microenvironment into one that supports healing.

2.7 AsCu@Gel synergistically enhances osteoinduction and suppresses inflammatory signaling in *Staphylococcal* osteomyelitis

The AsCu@Gel system demonstrated potent osteoinductive and anti-inflammatory properties. MC3T3 cells treated with AsCu@Gel showed significantly increased ALP activity (2.1-fold, **Figure 6B**) and mineralized nodule formation (1.8-fold, **Figure 6A**) versus controls. In LTA-stimulated RAW264.7 cells **(Figure 6C–H)**, AsCu@Gel upregulated AKT1 (3.2-fold) while suppressing inflammatory markers (MAPK8↓52%, MMP-9↓83%, SRC↓71%, TLR9↓68%, IDO1↓62%). Immunofluorescence **(Figure 6I and J)** confirmed significant reduction of iNOS (91%) and CSF1R (98%), with parallel AKT1 upregulation (4.1-fold) and SOX-9 ablation (99%), indicating a shift from chondrogenic to osteogenic repair pathways **(Figure S8A–F)**.

2.7.1 AsCu@Gel upregulates osteogenic markers *in vivo* and *in vitro*, indicating functional bone matrix maturation

To elucidate the osteoinductive mechanism of AsCu@Gel at the molecular level, immunohistochemical (IHC) staining was performed for key osteogenic markers, osteocalcin (OCN) and osteopontin (OPN), on decalcified femoral sections from an *in vivo* osteomyelitis model. AsCu@Gel treatment resulted in a significant increase in both OCN and OPN-positive areas compared to all control groups (**Figures S9A and S9B**). Quantitative analysis revealed the highest expression in the AsCu@Gel group (OCN: 23%; OPN: 19%). These results indicate robust osteoblast activity and accelerated deposition of functional bone matrix in situ, consistent with active mineralization during bone repair [71, 72]. In support of these *in vivo* findings, qRT-PCR analysis demonstrated that AsCu@Gel extract significantly upregulated the mRNA expression of OCN, OPN, and RUNX2 in MC3T3 pre-osteoblasts under LTA-stimulated conditions (**Figure S9E–G**). RUNX2, a master transcriptional regulator of osteoblast differentiation [73], was markedly elevated, confirming activation of the core osteogenic program. The coordinated upregulation of OCN and OPN, which are critical non-collagenous proteins regulating hydroxyapatite crystallization and collagen fibrillogenesis [74], further underscores the functional relevance of AsCu@Gel in bone matrix maturation. Collectively, these findings demonstrate that AsCu@Gel not only restores bone mass but also enhances bone quality by promoting osteogenic differentiation and matrix maturation. The elevated expression of OCN and OPN is particularly significant, as both proteins are established biomarkers of osteoblast activity and are essential for bone mechanical competence [75].

2.8 *In vivo* biocompatibility and therapeutic efficacy of AsCu@Gel

The progression of osteomyelitis in this model is defined by specific time points. Peak neutrophilic infiltration occurs at day 3 , and by day 14, established disease is characterized by abscesses and osteonecrosis [76]. The period between days 7 and 10 is a critical therapeutic window, where immune exhaustion occurs, characterized by impaired neutrophil and macrophage function and heightened checkpoint marker expression [76]. Concurrently, bacteria evade host defenses through biofilm formation and secretion of immune-modulatory factors [83]. This failure of innate immunity allows for bacterial persistence and the maturation of biofilms.

Day 10 was selected as the primary endpoint to reflect the timing of mid-course clinical intervention. This time point allows for a robust assessment of therapeutic efficacy when both immune dysfunction and bacterial challenges are advanced but before the onset of irreversible osteonecrosis and abscess formation at day 14 [83]. Therefore, the model effectively mimics human disease, showing immune dysfunction and biofilm formation. Key outcomes include reduced abscess volume, preserved bone structure, and lower bacterial burden, underscoring its translational potential and relevance in early clinical scenarios.

After 10 days of implantation **(Figure S10)**, AsCu@Gel exhibited excellent biocompatibility with no signs of systemic toxicity. H&E staining of major organ sections (heart, liver, spleen, lungs, kidneys) showed normal histoarchitecture without inflammation, necrosis, or pathological lesions **(Figure 7A)**. Serum biochemical analysis confirmed hepatorenal safety, with alanine aminotransferase (ALT) (Control: 23.6±0.3 U/L vs. AsCu@Gel: 18.3±0.4 U/L, p=0.007), aspartate aminotransferase (AST) (Control: 87.1±3.0 U/L vs. Cu@Gel: 122.7±9.3 U/L vs. AsCu@Gel: 104.5±3.7 U/L, p=0.002), and creatinine (CREA) (Control: 16.1±0.5 μmol/L vs AsCu@Gel: 19.4±0.6 μmol/L, p=0.0005) levels all within physiological ranges **(Figure 7B)**. These results collectively demonstrate the *in vivo* safety profile of AsCu@Gel for therapeutic applications.

By day 10, pathological changes reach a quantitatively significant level, as indicated by measurable bacterial counts and distinct histopathological scores. However, these changes are not yet so severe that they obscure the beneficial effects of treatment. In contrast, at later stages, such as day 14 [77, 84], the high bacterial load and extensive tissue necrosis hinder the ability to differentiate between ineffective therapy and interventions that only slow disease progression. Demonstrating a positive outcome at day 10 proves that the intervention can halt and reverse infection progression.

AsCu@Gel resolves inflammation both systemically and locally, supporting the occurrence of macrophage reprogramming. To assess the translational immunomodulatory effects of this treatment, key pro-inflammatory cytokines were quantified in serum and bone marrow. The findings indicate that AsCu@Gel induces a significant anti-inflammatory response in both compartments. Systemic administration of AsCu@Gel resulted in a marked, stepwise reduction of TNF-α and IL-6 levels in serum, with statistically significant differences compared to all other treatment groups (Control, Gel, As@Gel, and Cu@Gel) **(Figure S11)**. This systemic anti-inflammatory effect was also observed, and was even more pronounced, in the bone marrow microenvironment, where TNF-α and IL-6 levels were lowest in the AsCu@Gel group. The coordinated suppression of pro-inflammatory mediators provides strong *in vivo* evidence for the proposed mechanism: the synergistic push-pull action of AsCu@Gel effectively suppresses the global

inflammatory cascade, extending beyond localized macrophage reprogramming to restore systemic immune homeostasis. Hematological analysis further supported the resolution of infection and inflammation, as the pronounced leukocytosis observed in the control and gel-only groups was effectively controlled by the treatments. The AsCu@Gel combination was the most effective, reducing the White Blood Cell (WBC) count to near-normal levels **(Figure S12)**. The concurrent decline in both systemic cytokine levels and leukocytosis demonstrates that AsCu@Gel simultaneously reduces the bacterial burden and suppresses the hyperactive immune response, thereby interrupting the pathogenic cycle of acute osteomyelitis.

2.9 AsCu@Gel eradicates *Staphylococcus aureus* infection and preserves bone integrity in implant-associated osteomyelitis

To evaluate AsCu@Gel's efficacy in treating acute *Staphylococcal* osteomyelitis (AOM), we used a mouse model of implant-associated osteomyelitis. After three days, the implant was removed, and the defect was filled with hydrogels, with tissues collected ten days post-implantation **(Figure S13)**. Radiological analysis revealed no significant bone destruction or structural irregularities in AOM mice at this time point **(Figures S13 and S14)**, aligning with prior studies [87-89]. Treatment with AsCu@Gel resulted in near-sterilization of bone and adjacent soft tissues, as confirmed by bacterial cultures, a significant improvement over the other four groups **(Figures 8A–C)**. H&E staining further confirmed these results: while the control group exhibited deep purple staining (indicating *S. aureus* colonization around the implant and femur), the AsCu@Gel group displayed smaller, well-demarcated infection sites, minimal tissue damage, and near-absence of abscesses or necrotic cells **(Figure 8D)**. Overall, these findings demonstrate AsCu@Gel's therapeutic potential in alleviating AOM symptoms by reducing bacterial burden and preserving tissue integrity.

Immunohistochemical analysis of decalcified femur slices at day 10 post-surgery revealed dynamic modulation of macrophage polarization markers in bone and muscle tissues **(Figure S15)**. LSD1 and MMP-9 **(Figure S15A, C)**, markers of pro-inflammatory M1 macrophages, exhibited significant downregulation in all treatment groups (Gel, As@Gel, Cu@Gel, AsCu@Gel) compared to Control ($p < 0.01$ for LSD1; $p < 0.05$ for MMP-9, **Figure S15E, G**). The AsCu@Gel group showed the most pronounced reduction (62% for LSD1; 49% for MMP-9), indicating robust inhibition of M1 polarization. While, CSF1R **(Figure S15B)**, a key M2 marker, was elevated across treatments, with AsCu@Gel demonstrating a 4-fold increase versus Control ($p < 0.05$, **Figure S15F**). Variability in As@Gel (e.g., one outlier replicate) suggested context-dependent effects. Also, SOX-9 **(Figure S15D)**, another M2-associated marker, was upregulated in AsCu@Gel (14% increase vs. Control; $p < 0.01$, **Figure S15H**), further supporting enhanced M2 polarization. Furthermore, quantitative analysis confirmed that AsCu@Gel most effectively skewed macrophage polarization from pro-inflammatory M1 to anti-inflammatory/reparative M2 phenotypes **(Figure S15E–H)**. This dual effect suppression of M1 markers (LSD1, MMP-9) and upregulation of M2 markers (CSF1R, SOX-9) highlights the potential of AsCu@Gel to mitigate inflammation while fostering tissue repair.

Compared to conventional treatments like non-biodegradable poly (methyl-methacrylate) (PMMA) antibiotic beads [90, 91], the AsCu@Gel system offers several advantages. First, it provides a spatiotemporally controlled release of both antibacterial and immunomodulatory agents, overcoming the issues of burst release and limited drug availability often seen with PMMA. Second, AsCu@Gel is biodegradable, eliminating the need for a second surgical removal procedure. Third, it enables triple-mode therapy, which is antibacterial, immunoregulatory, and osteogenic, rather than just delivering antibiotics.

Recent advances in immunomodulatory bone repair materials highlight a growing emphasis on host immune reprogramming. Zinc-ion-doped hydrogels, for instance, promote M2 macrophage polarization and enhance osteogenesis, whereas magnesium-based scaffolds modulate inflammatory responses and stimulate bone regeneration [92, 93]. However, most current systems do not simultaneously provide both antibacterial and immunomodulatory effects [94]. Natural product-composite hydrogels, such as those incorporating curcumin or quercetin, confer anti-inflammatory properties but exhibit limited antibacterial activity against persistent biofilms [94]. In contrast, AsCu@Gel combines *As*'s reactive oxygen species (ROS)-scavenging and immunomodulatory capabilities with the broad-spectrum antibacterial and osteogenic properties of Cu^{2+}, thereby enabling simultaneous targeting of infection, inflammation, and bone loss. Such a combinatorial approach is seldom realized in single-platform designs. Additionally, compared to other copper-delivery systems, including Cu-doped bioactive glasses and Cu-MOFs, AsCu@Gel exhibits superior responsiveness to microenvironmental stimuli such as pH, enzymes, and temperature, which facilitates precise delivery within the acidic, enzyme-rich environment of an infection [98-101]. This multi-stimuli responsiveness aligns with the emerging paradigm of smart immunomodulatory biomaterials that detect and respond to pathological cues [102].

Despite these advances, several limitations of the AsCu@Gel platform warrant consideration. Although this study demonstrates potent antibacterial activity and a membrane-disruption mechanism, morphological analysis using scanning or transmission electron microscopy (SEM/TEM) and quantification of bacterial metabolic activity through ATP assays were not performed. These techniques could have provided ultrastructural details of membrane damage and additional evidence of cellular metabolic collapse, thereby offering a more comprehensive mechanistic understanding. Nevertheless, the conclusions are supported by a robust multimodal evidence chain, including quantitative bacterial growth inhibition (OD_{600}), direct visualization of membrane integrity loss via SYTOX Green fluorescence imaging, and comprehensive *in vivo* biocompatibility assessment confirming the material's safety profile.

Furthermore, while enhanced osteogenic differentiation and bone matrix deposition were demonstrated, direct biomechanical validation, such as three-point bending tests, was not conducted. Biomechanical testing remains the gold standard for assessing functional bone restoration. However, the combination of microstructural (Micro-CT), protein-level (IHC), and transcriptional (qPCR) data provides compelling multi-parametric evidence that AsCu@Gel promotes both bone mass and bone quality. The upregulation of OCN and OPN, key regulators of mineralization and collagen organization, strongly suggests improved bone matrix integrity, which is a fundamental determinant of mechanical strength [103, 104]. Additional limitations include the long-term degradation behavior and potential *in vivo* accumulation of the hydrogel, which require further investigation. The complexity of nanocomposite synthesis may also pose challenges for large-scale clinical translation. Future studies should explore chronic infection models with established biofilms and employ single-cell RNA sequencing to elucidate immune cell heterogeneity in response to treatment. In summary, while these limitations are acknowledged, the findings robustly support the therapeutic potential of AsCu@Gel. Future work incorporating SEM/TEM, ATP assays, biomechanical testing, and deeper investigation into synergistic ion-release kinetics will further solidify the mechanistic understanding and advance the translational potential of this composite hydrogel platform.

3.Conclusion

This study successfully introduces a new therapeutic approach for AOM by shifting from the passive delivery of antibiotics to the active design of immunomodulatory biomaterials. The AsCu@Gel platform demonstrates that a coordinated triple-action strategy, simultaneously eliminating biofilms, reprogramming the host immune response, and promoting bone regeneration, is essential for breaking the chronic cycle of the disease. The core innovation of this research lies in the synergistic nano-immunomodulation between astaxanthin and copper, which effectively polarizes macrophages from a destructive M1 phenotype to a regenerative M2 phenotype. By combining targeted antibacterial effects with foundational immune reprogramming, AsCu@Gel successfully disconnects the link between infection and tissue damage. Overall, this study not only presents a highly effective and translatable platform but also positions active immune reprogramming as a central principle for designing the next generation of therapies aimed at complex inflammatory diseases.

4.Experimental Section

4.1 Materials and reagents

Astaxanthin (*As*) and lipopolysaccharide (LPS) were purchased from Sigma-Aldrich (St. Louis, MO, USA). Copper chloride was obtained from Chemical Reagent Co., Ltd. (Guangzhou, China). DSPE-PEG_{2000} and other analytical-grade reagents were purchased from Aladdin (Shanghai, China). N,N-Dimethylformamide (DMF) was obtained from Shanghai Macklin Biochemical Co., Ltd. The Apoptosis Analysis Kit, BCIP/NBT ALP Color Development Kit, CCK-8 detection kit, and calcein-AM/propidium iodide (PI) were purchased from Beyotime Institute of Biotechnology (Shanghai, China). The Alizarin Red staining kit was obtained from Beijing Reagan Biotechnology. The murine macrophage cell line RAW264.7 (Research Resource Identifier [RRID]: CVCL_0493, Cellosaurus) was obtained as a cryopreserved, ready-to-culture stock (Product Number C7505) from Beyotime Biotechnology. According to the supplier's specifications, the cell line was confirmed to be free of mycoplasma contamination. Dulbecco's Modified Eagle's Medium (DMEM) was acquired from Gibco (Thermo Fisher Scientific, Waltham, MA, USA). Fetal bovine serum was purchased from ExCell Biochemical. The fluorescent probes 2,7-dichlorodihydrofluorescein diacetate (DCFH-DA) and crystal violet staining kit were obtained from Solarbio Biochemical. The RNA extraction kit was purchased from Accurate Biology (Hunan, China). Phalloidin-TRITC and 5-ethynyl-2′-deoxyuridine (EdU) kit were purchased from YEASEN Biochemical (Shanghai, China). The Hematoxylin and Eosin (H&E) staining kit was obtained from Leagene. Primary antibodies (anti-CSF1R, anti-MMP-9, anti-SOX-9, anti-TLR9, anti-AKT1, anti-Src, anti-iNOS, and anti-LSD1) and secondary antibodies (goat anti-rabbit IgG and goat anti-mouse IgG) were purchased from Affinity Biosciences. Alexa Fluor 488/594/700-conjugated secondary antibodies were obtained from Thermo Fisher Scientific. Fluoroshield mounting medium with DAPI and neutral balsam were acquired from Sigma-Aldrich and Sangon Biotech, respectively. The synthesis of HPCH was performed as previously described [105].

4.2 Preparation of of *As*-copper nanoparticles (AsCu NPs)

Three nanoparticle (NP) batches were formulated by dissolving As (3–45 mg), $CuCl_2$ (6–60 mg), and DSPE-PEG_{2000} (6–60 mg) in DMF (1–6 mL) under magnetic stirring (500 rpm, 30 min, 40°C). The organic phase was then mixed with distilled water (20–60 mL) and stirred for 30 min at 40°C to induce nanoprecipitation via self-assembly [106]. The amphiphilic DSPE-PEG_{2000} was selected for its dual function: 1) Steric stabilization: PEG chains prevent NP aggregation by forming a hydrophilic corona [107] and 2) Stealth properties: PEGylation extends systemic circulation by reducing opsonization [108]. The mixture was transferred into dialysis membranes (BS-QT-022) and immersed in 2 L of distilled water (pH 5.5–6.5) under dark conditions to prevent *As* photodegradation. The water was replaced every 2 h for the first 24 h (to remove >99% DMF) [109], then daily for 72 h total to ensure complete DMF removal (validated by GC-MS; residual DMF < 100 ppm) , while the DMF/water ratio (1:20-1:10) controlled NP size [111, 112]. Finally, the dialyzed solution was freeze-dried to obtain a stable AsCu NP powder.

4.3 Characterizations of AsCu NPs and HPCH hydrogels

The morphology of AsCu NPs was examined by transmission electron microscopy (TEM) (HT7800, Hitachi TEM system, Japan). Hydrated particle size was determined by a Brookhaven 90Plus DLS instrument (Brookhaven, USA). AsCu NP suspension (20 mg/mL in PBS) was used for thermogravimetric analysis (TGA) on a Mettler TGA/DSC 3+ (Switzerland). The X-ray photoelectron spectroscopy (XPS) analysis for the elements copper (Cu2p), carbon (C1s), nitrogen (N1s), oxygen (O1s), and phosphorus (P2p) in the context of $AsCu^{2+}$-loaded DSPE-PEG_{2000} nanoparticles provides detailed information about the chemical states and composition of the nanoparticles using Thermo Scientific™ K-Alpha (USA).

A hydrogel composite was prepared by dissolving 40 mg of hydroxypropyl chitin (HPCH) in 2 mL of PBS containing 20 mg of AsCu NPs and stored overnight at 4°C to ensure complete dissolution. Gelation was induced by incubating at 37°C for 30 min, forming a stable hydrogel matrix. The hydrogel was immersed in 2500 mL of PBS (pre-warmed to 37°C) and incubated under gentle agitation (100 rpm) in a temperature-controlled shaker to simulate physiological conditions. Sink conditions were maintained throughout the experiment to avoid saturation effects. At predetermined time intervals (1, 3, 6, 24, 48, and 72 h; 5 and 7 days), 250 μL aliquots of the release medium were collected and transferred to 1.5 mL EP tubes containing 200 μL of chloroform (to prevent NP aggregation and preserve sample integrity) [113]. Then, samples were immediately stored at −20°C until analysis. After 7 days, all samples were thawed and vigorously mixed using a vortex mixer (30 sec) to ensure homogeneity. A 100 μL aliquot from each time point was transferred to a 96-well plate, and the concentration of released AsCu NPs was quantified using a fluorescence microplate reader at 490 nm. Release kinetics were fitted to Higuchi, Korsmeyer-Peppas, and zero/first-order models to elucidate diffusion mechanisms [114, 115].

The release kinetics of Cu^{2+} from AsCu@Gel nanocomposites were evaluated using a dialysis method under simulated physiological (37 °C) and mild hyperthermic (40 °C) conditions, representing normal body temperature and therapeutic hyperthermia, respectively. Samples (1 mL of 1 mg/mL Cu^{2+}) were sealed in pre-hydrated dialysis bags with a 3.5 kilodalton (kDa) molecular weight cut-off. These bags were immersed in 50 mL of PBS maintained at either 37 °C or 40 °C under constant agitation. At a given time point (0, 1, 3, 6, 12, 24, 48, and 72 h), 1 mL aliquots were withdrawn from the release medium and replaced with an equal volume of fresh, pre-warmed PBS to maintain sink conditions. After that, the concentration of Cu^{2+} in the collected aliquots was quantified using inductively coupled plasma mass spectrometry. Finally, the cumulative percentage of Cu^{2+} released was calculated and plotted as a function of time for each formulation and temperature. To assess enzyme-mediated release, the procedure was repeated using PBS containing 100 μg/mL hyaluronidase.

The thermoresponsive rheological properties of AsCu@Gel were evaluated using a rotational rheometer (Discovery HR30, TA Instruments, USA) with a 20 mm parallel plate geometry.

Temperature sweep measurements were conducted from 13 °C to 37 °C at a constant frequency of 1 Hz and a strain of 1% to assess the storage modulus (G′), loss modulus (G″), and loss tangent (tan). Frequency sweep measurements were performed at 37 °C across an angular frequency range of 0.6 to approximately 600 rad/s (strain 1%) using an 8 mm parallel plate geometry. All experiments were performed in triplicate.

4.4 *In vitro* antibacterial assays

S. aureus was isolated from a patient diagnosed with AOM in our department [84, 116]. The bacterial suspension was adjusted to an optical density at 600 nm (OD_{600}) of 0.5, corresponding to a concentration of 1 × 10^8 CFU/mL. The hydrogel formulations consisted of plain HPCH (Gel), astaxanthin-only (As@Gel), copper-only (Cu@Gel), and mixed astaxanthin/copper ratios (1/3 and 2/3) to evaluate potential synergistic effects. The HPCH-only group functioned as a negative control to eliminate matrix-related antibacterial activity. Hydrogel samples of 200 μL were incubated with 1 mL of the bacterial suspension in 1.5 mL centrifuge tubes at 37°C with agitation at 100 rpm. At specific time points (1, 3, and 7 days), 300 μL aliquots were collected, serially diluted in sterile PBS, and analyzed using a fluorescence microplate reader set to 600 nm. The *in vitro* bactericidal effects of the different hydrogels were assessed using the bacterial colony formation counting method.

4.4.1 Bacterial membrane integrity assay (SYTOX Green staining)

Bacterial membrane integrity was evaluated using the SYTOX Green nucleic acid stain. After 24 h of co-culture with hydrogels, *S. aureus* cells were washed with PBS, stained with SYTOX Green (1 μM for 15 min in the dark), and imaged using a fluorescence microscope (NIKON). The presence of green fluorescence signified compromised membrane integrity and nucleic acid leakage.

4.5 *In vitro* biofilm formation assays

Staphylococcus aureus (isolated from an acute osteomyelitis case) was grown in the Mueller-Hinton broth to mid-log phase (OD_{600} = 0.5, 10^8 CFU/mL). Bacterial lawns were prepared by swabbing standardized suspensions onto Mueller-Hinton agar plates. Six-millimeter wells were aseptically punched in the agar and filled with 50 μL of hydrogel samples. Following a 2 h pre-diffusion period at 4°C to allow compound diffusion, plates were incubated at 37°C for 24 h. Inhibition zones were measured in triplicate using ImageJ (Version: 1.54g) with scale calibration against a reference ruler, ensuring ±0.1 mm precision. Additionally, *S. aureus* viability post 24 h hydrogel co-culture was evaluated using calcein-AM/PI staining (2 μM/1 μM, 37°C, 60 min, dark). The results were then observed under a fluorescence microscope (NIKON).

Hydrogel samples (100 μL) were incubated in 96-well plates (37°C, 30 min), followed by co-culture with *S. aureus* (OD_{600} = 0.2 in TSB medium) for 12 h. Bacterial viability was assessed by measuring absorbance at 600 nm. The bacterial suspension was transferred to fresh plates to evaluate biofilm formation, incubated in TSB (0.2 mL, 48 h), and fixed with 10% methanol. Biofilms were stained with 0.1% crystal violet (20 min), imaged microscopically, and quantified after dissolving in 33% acetic acid (absorbance at 590 nm).

4.5.1 Macrophage stimulation with LPS and LTA

Inflammatory activation relevant to both canonical TLR4 signaling and *Staphylococcus aureus*-specific TLR2 pathways was modeled by stimulating RAW264.7 macrophages with either LPS (1 μg/mL) or LTA (1 μg/mL) for 24 h prior to hydrogel treatment. LPS served as a standard high-potency agonist to establish a robust pro-inflammatory (M1) baseline, whereas LTA was selected to ensure pathological relevance to Gram-positive osteomyelitis.

4.6 *In vitro* cytotoxicity (CCK8)

RAW 264.7 cells (1×10^4/well) were seeded in 96-well plates to assess viability after 24 h incubation with hydrogels and AsCu. Post-incubation, 10 μL CCK-8 was added, followed by 2 h incubation at 37 °C. Absorbance (450 nm) was measured using a Thermo Fisher Varioskan Flash multimode reader to generate cytotoxicity curves.

4.7 Biocompatibility assay

Chondrocytes (1×10^4 cells/well) were cultured with sterilized hydrogels (24 h), fixed with 4% PFA (15 min), permeabilized with 0.5% Triton X-100 (15 min), and stained with Phalloidin-TRITC (1% BSA, 30 min) and DAPI. RAW 264.7 cells were similarly treated, then activated with *S. aureus* (1 h) before viability staining with calcein-AM/PI (1 μM/0.5 μM, 45 min, dark). Fluorescence images (NIKON) were quantified using ImageJ (Version: 1.54g). For hemocompatibility testing, mouse blood was incubated with hydrogels (37°C, 60 min), centrifuged, and supernatant absorbance (OD_{540}) measured to calculate hemolysis rates.

4.8 Network pharmacology approach to identify *As* targets in acute *Staphylococcal* osteomyelitis (AOM)

As target prediction and AOM-related gene screening were performed using cheminformatics. *As* data were retrieved from PubChem (https://pubchem.ncbi.nlm.nih.gov/), and 100 pharmacological targets were predicted via SwissTargetPrediction (http://swisstargetprediction.ch/). AOM-related genes were extracted from GeneCards (https://www.genecards.org/). Intersecting targets were identified using the "Venn Diagram" package in R 4.5.0. These overlapping genes were analyzed in Cytoscape (v3.9.1) using the "Bisogenet" plugin to construct a protein-protein interaction (PPI) network. This approach elucidates potential therapeutic targets of *As* in AOM pathogenesis, providing a foundation for further mechanistic investigation.

4.9 Gene ontology (GO) and kyoto encyclopedia of genes and genomes (KEGG) pathway enrichment analyses

The GO (http://GeneOntology.org/) and KEGG (https://www.kegg.jp/kegg/) pathway enrichment analyses were performed on intersected target genes using R packages ("colorspace," "stringi," "ggplot2") and Bioconductor tools ("DOSE," "clusterProfiler," "enrichplot"). The organism was set to "hsa" with thresholds of $p < 0.05$ and $q < 0.05$. GO analysis categorized results into cellular components (CC), biological processes (BP), and molecular functions (MF), while KEGG identified key pathways. Enrichment results were visualized as bubble plots, highlighting significant terms. The "clusterProfiler" and "ggplot2" packages facilitated functional annotation with stringent filtering (p and $q < 0.05$) to ensure robustness. Bubble charts summarized enriched terms, illustrating *As*'s potential mechanisms in AOM pathogenesis through CC, BP, and MF insights. This systematic approach clarifies the pharmacological roles of *As*-targeted genes in osteomyelitis.

4. 10 5-Ethynyl-2'-deoxyuridine (EdU) staining protocol

Chondrocyte proliferation was evaluated utilizing the Yefluor 488 EdU Cell Imaging Kit. For macrophage experiments, RAW264.7 cells were stimulated with LPS or LTA as described in Section 4.5.1, followed by hydrogel treatment. Initially, the cells were labeled with a 10 μM EdU working solution for 2 h. Following this labeling step, the cells were fixed in 4% paraformaldehyde (PFA) for 30 min and subsequently neutralized using 50 μL of a 2 mg/mL glycine solution for 5 min. The cells underwent two washing steps using a 3% bovine

serum albumin (BSA) solution in phosphate-buffered saline (PBS). Subsequently, they were incubated with 0.5% Triton X-100 for 10 min. Following this incubation, the cells received 100 μL of the Click-iT reaction mixture along with Hoechst (a nuclear stain) and were maintained at 37°C in the dark for 30 min. Finally, we analyzed the cells using a NIKON fluorescence microscope.

4.11 Reactive oxygen species (ROS) assay

RAW264.7 cells were seeded onto 96-well plates (1×10^4 cells per well) and stimulated with either LPS (1 μg/mL) or LTA (1 μg/mL) for 24 h prior to hydrogel co-culture. Reactive oxygen species (ROS) levels in living cells were quantified using a ROS Assay Kit. Cells were then co-cultured with hydrogels for 24 h prior to collection. Following the instructions provided by the kit, a basal medium containing Dichlorodihydrofluorescein diacetate (DCFH-DA) (1 μL/mL, 10 μM) was introduced to resuspend the cells, followed by an incubation period of 30 min. Subsequently, the cells were subjected to three wash cycles with RPMI-1640 medium to eliminate residual DCFH-DA. Ultimately, the results were assessed using a fluorescence microplate reader, and the cellular samples were examined under a fluorescence microscope (NIKON) and quantified using GraphPad Prism 10.1.2.

4.12 Apoptosis detection by flow cytometry assays

RAW264.7 cells (1×10^5 cells/well) were seeded in 6-well plates and stimulated with either LPS (1 μg/mL) or LTA (1 μg/mL) for 24 h to induce pro-inflammatory activation through TLR4 or TLR2 signaling, respectively. After stimulation, the cells were treated with hydrogels for an additional 24 h. Cells were then harvested, resuspended in PBS (500 μL), and stained with FITC-Annexin V/PI (5 μL each). Apoptosis was analyzed by flow cytometry (FlowJo v10) and quantified using GraphPad Prism 10.1.2. All experiments were performed in triplicate.

4.13 RNA extraction and RT-qPCR analysis

Total RNA was isolated from LPS or LTA-stimulated RAW264.7 cells using AG RNAex Pro Reagent, followed by cDNA synthesis with the PrimeScript™ RT reagent kit. The quantitative PCR was performed with SYBR Green Master Mix (Yeasen Biotechnology) using gene-specific primers (**Table S4**). Gene expression was calculated via the 2-ΔΔCT method with GAPDH as endogenous control. All reactions were performed in technical triplicates.

4.14 Western Blot Analysis

RAW264.7 cells (1×10^5 cells per well) were seeded in 6-well plates and stimulated with LPS (1 μg/mL) for 24 h, followed by hydrogel treatment for an additional 24 h. Cells were lysed in RIPA buffer containing protease and phosphatase inhibitors. Following centrifugation, protein concentrations were measured using the BCA assay. Proteins (20–30 μg) were separated by SDS-PAGE and transferred to PVDF membranes. Membranes were blocked with 5% non-fat milk and incubated overnight at 4°C with primary antibodies targeting TLR9, phospho-TLR9, JNK, phospho-JNK, AKT, phospho-AKT, and GAPDH. After incubation with HRP-conjugated secondary antibodies, bands were visualized using enhanced chemiluminescence (ECL) and quantified. Phosphoprotein levels were normalized to total protein, and total protein levels were normalized to GAPDH. Data are presented as mean ± SD from three independent experiments.

4.15 Osteogenic differentiation culture conditions

MC3T3 cells were cultured in osteogenic differentiation medium containing DMEM supplemented with 10% FBS, 50 μg/mL ascorbic acid, 10 mM β-glycerophosphate, and 100 nM dexamethasone during mineralization and alkaline phosphatase (ALP) assays.

4.16 Alizarin red S staining

MC3T3 cells (1×10^5 cells/well) were cultured in osteogenic differentiation medium, LPS-stimulated (1 μg/mL) and treated with hydrogels to assess mineralization. After 7 days, cells were fixed with 4% formaldehyde (10 min, RT), washed with PBS, and stained with alizarin red S (15 min, RT). Following thorough washing with ddH_2O, mineralization deposits were visualized and imaged by fluorescence microscopy.

4.17 Alkaline phosphatase (ALP)

Alkaline phosphatase (ALP) was assessed in MC3T3 cells (1×10^5 cells/well) cultured in osteogenic differentiation medium, following LPS stimulation (1 μg/mL) and hydrogel treatment. After 7 days of culturing, cells were stained using a BCIP/NBT ALP detection kit according to manufacturer protocols. Stained samples were captured under a fluorescence microscope. Experiments were conducted in triplicate. This assay provided an evaluation of early osteogenic differentiation potential under experimental conditions.

4.18 Immunofluorescence staining

Deparaffinized and rehydrated slides underwent antigen retrieval in Tris-EDTA buffer (pH 9.0, 75°C, 45 min). Sections were blocked with 5% BSA (30 min, RT) and incubated with primary antibodies (AKT1, iNOS, MMP-9, CSF1R, SOX-9, SRC; 1:500 in 5% BSA/PBS, 4°C overnight). After washing, sections were incubated with Alexa Fluor-conjugated secondary antibodies (488/594/700; 1:1000) for 1 h. Multiplex immunofluorescence was performed using a tyramide signal amplification kit (AFIHC026, Aifang Biological) per manufacturer's protocol. Nuclei were counterstained with Hoechst 33342 (1:1000, 10 min). Fluorescence images were acquired using a NIKON microscope under consistent exposure settings. The quantitative analysis of fluorescence intensity was performed using ImageJ (Version: 1.54g), with background subtraction and normalization to the Hoechst signal.

4.19 Animal model

Male C57BL/6J mice (6-12 weeks, Southern Medical University) were randomly divided into five groups (n=8/group) following approval by the Institutional Animal Ethics Committee: (1) Infected, untreated Control; (2) Gel-only; (3) As@Gel; (4) Cu@Gel; and (5) AsCu@Gel. Animals were housed under controlled conditions (12h light/dark cycle, 18-22°C, 50-60% humidity) with ad libitum access to food/water. An implant-associated AOM model was established by creating a 0.5 mm femoral defect, injecting 2 μL *S. aureus* suspension (1×10^8 CFU/mL), and fixing with a sterile screw (1×2 mm). After 72h, implants were removed, and defects were filled with hydrogels. Tissues were harvested 10 days post-implantation for: (1) X-ray and Micro-CT analysis (Bruker Skyscan 1276); (2) Quantitative bacterial culture of bone/soft tissue; (3) Histopathological evaluation (H&E staining); (4) Immunohistochemical analysis of inflammatory markers. The heart, liver, spleen, lung, kidneys and blood were collected for systemic toxicity assessment. All procedures complied with ARRIVE guidelines and the National Research Council's Guide for Care and Use of Laboratory Animals.

4.20 Blood collection and analysis

Cardiac puncture under tribromoethanol anesthesia (250 mg/kg, i.p.) yielded 1.5-2.0 mL blood samples. The serum was isolated by centrifugation (2,000 rpm, 10 min) and analyzed using a clinical chemistry analyzer for biochemical profiling. Systemic and local concentrations of the pro-inflammatory cytokines TNF-α and IL-6 were quantified using commercial mouse ELISA kits (Neobioscience, China). Serum samples were collected and analyzed without further processing. Bone

marrow tissues were harvested, weighed, homogenized in PBS, and centrifuged at 12,000 rpm for 20 min at 4°C. The resulting supernatant was used for cytokine analysis. All procedures were conducted in accordance with the manufacturer's protocols.

4.21 Histological analysis

The mouse heart, liver, spleen, lungs, kidneys, and right legs were fixed in 4% paraformaldehyde for 24 h. Bone specimens with soft tissues underwent decalcification in 10% EDTA (10%, 2 weeks), followed by paraffin embedding. Sections (5 μm) were stained with H&E and imaged by light microscopy (NIKON). All procedures followed institutional animal care guidelines.

4.22 Immunohistochemical analysis

Deparaffinized sections underwent antigen retrieval (EDTA, pH 6.8, 70°C, 60 min), peroxidase blocking (0.3% H_2O_2, 30 min), and serum blocking (1 h). Firstly, primary antibodies were applied overnight at 4°C (rabbit anti-CSF1R [1:200, Affinity Biosciences AF0080, RRID: AB_2833269], anti-MMP-9 [1:200, Affinity Biosciences AF5228, RRID: AB_2837714], anti-SOX-9 [1:200, Affinity Biosciences AF6330, RRID: AB_2835186], anti-OCN (1:200, Abcam ab93876, RRID:AB_10675156), anti-OPN (1:200, Santa Cruz sc-21742, RRID:AB_627664), and anti-RUNX2 (1:200, Cell Signaling #12556, RRID:AB_10949326); mouse anti-LSD1 [1:200, Affinity Biosciences BF0551, RRID: AB_2833566]). After secondary antibody incubation (RT, 60 min), chromogenic development was performed. Slides were imaged at 200× magnification (NIKON) with isotype controls (Goat anti-Rabbit IgG [1:500-1:1000, Affinity Biosciences S0001, RRID: AB_2833231] and Goat anti-Mouse IgG [1:500-1:1000, Affinity Biosciences S0002, RRID: AB_2833232]) and omission controls for validation. Slides were imaged by light microscopy, and quantitative analysis of staining intensity was performed using ImageJ (Version: 1.54g).

4.23 *In vivo* antibacterial assay

Ten days post-implantation, mice were euthanized, and right femurs with adjacent soft tissues were harvested. Tissues were homogenized in PBS (0.1 mg/μL), serially diluted (10^1–10^5), and 10 μL aliquots were plated on TSA agar. After a 20-h incubation at 37°C, the bacterial colonies were counted and reported as $\log_{10}$ CFU/g of tissue (mean ± SD).

4.24 X-ray microscopic 2D imaging and micro-CT analysis

Ten days post-implantation, mouse femurs were fixed in 4% paraformaldehyde for 24 h and scanned using a Bruker Skyscan 1276 system (Kontich, Belgium). The scan parameters were as follows: voxel size, 6.53 μm; resolution, medium; voltage, 70 kV; current, 200 μA; filter, 0.25 mm Al; and integration time, 350 ms. Density measurements were calibrated using the manufacturer's calcium hydroxyapatite (CaHA) phantom. Image reconstruction was performed with NRecon (v1.7.4.2), and 3D images were generated from contoured 2D images using a grayscale distance transformation algorithm (CTvox, v3.3.0). Both 2D and 3D analyses were conducted using CT Analyser (v1.20.3.0). Bone microarchitecture was evaluated within a defined region of interest (ROI), with the following parameters assessed: bone mineral density (BMD), bone volume fraction (BV/TV), trabecular thickness (Tb.Th), trabecular number (Tb.N), trabecular separation (Tb.Sp), structure model index (SMI), bone surface/volume ratio (BS/BV), intersection surface (i.S), and trabecular pattern factor (Tb.Pf).

4.25 Statistical analysis

Data analysis and graphical representations were carried out using IBM SPSS (v24.0), GraphPad Prism (v10.1.2), R (v4.5.0), and BioRender. The results are reported as mean ± SD from three or more independent experiments. Between-group comparisons were conducted using Student's t-test (applicable to both parametric and non-parametric data), while multiple comparisons were assessed using one-way or two-way ANOVA followed by Tukey's post-hoc test. Significance levels were designated as *p<0.05, **p<0.01, ***p<0.001, and ****p<0.0001 compared to control groups.

Data availability

All data needed to support the conclusions in the paper are presented in the manuscript and/or the Electronic Supplementary Material. Additional data related to this paper may be requested from the corresponding author upon request.

Acknowledgements

This work was supported by the National Key Research and Development Program of China (2022YFC2504305).

Declaration of competing interest

All the contributing author(s) report(s) no conflict of interests in this work."

Author contribution statement

V.T.M.: Conceptualization, Methodology, Software, Formal analysis, Investigation, Writing & original draft preparation. **Y.P.L.**: Methodology, Formal analysis, Investigation, Data curation, Writing review & editing. **H.T.W.**: Methodology, Software, Validation, Investigation, Resources. **B.Y.**: Writing review & editing, Supervision. **D.G.G.**: Validation, Resources, Writing review & editing, Supervision. **J.W.**: Validation, Visualization, Supervision, Project administration. **B.Y.**: Validation, Supervision, Project administration, Funding acquisition.

Informed consent

Not applicable.

Ethics statement

The animal experiments were carried out following the guidelines of the Southern Medical University-Nanfang Hospital Institutional Committee for the Care and Use of Laboratory Animals and were approved by the Committee on Ethical Use of Animals of Southern Medical University (Ethical code: SMUL202512001).

Use of AI statement

"None."

References

[1] Bury, D. C.; Rogers, T. S.; Dickman, M. M. Osteomyelitis: Diagnosis and Treatment. *Am. Fam. Physician.* **2021**, *104*, 395-402.

[2] Lew, D. P.; Waldvogel, F. A. Osteomyelitis. *Lancet* **2004**, *364*, 369-379.

[3] Masters, E. A.; Ricciardi, B. F.; Bentley, K.; Moriarty, T. F.; Schwarz, E. M.; Muthukrishnan, G. Skeletal infections: microbial pathogenesis, immunity and clinical management. *Nat. Rev. Microbiol.* **2022**, *20*, 385-400.

[4] Urish, K. L.; Cassat, J. E. Staphylococcus aureus Osteomyelitis: Bone, Bugs, and Surgery. *Infect. Immun.* **2020**, *88*.

[5] Lee, J. H.; Baik, J. M.; Yu, Y. S.; Kim, J. H.; Ahn, C. B.; Son, K. H.; Kim, J. H.; Choi, E. S.; Lee, J. W. Development of a heat labile antibiotic eluting 3D printed scaffold for the treatment of osteomyelitis. *Sci. Rep.* **2020**, *10*, 7554.

[6] Zegre, M.; Poljanska, E.; Caetano, L. A.; Goncalves, L.; Bettencourt, A. Research progress on biodegradable polymeric platforms for targeting antibiotics to the bone. *Int. J. Pharm.* **2023**, *648*, 123584.

[7] Wang, Y.; Zhang, W.; Yao, Q. Copper-based biomaterials for

bone and cartilage tissue engineering. *J. Orthop. Transl.* **2021**, *29*, 60-71.

[8] Lin, Z.; Cao, Y.; Zou, J.; Zhu, F.; Gao, Y.; Zheng, X.; Wang, H.; Zhang, T.; Wu, T. Improved osteogenesis and angiogenesis of a novel copper ions doped calcium phosphate cement. *Mater. Sci. Eng. C-Mater. Biol. Appl.* **2020**, *114*, 111032.

[9] Ameh, T.; Sayes, C. M. The potential exposure and hazards of copper nanoparticles: A review. *Environ. Toxicol. Pharmacol.* **2019**, *71*, 103220.

[10] Valentino, A.; Yazdanpanah, S.; Conte, R.; Calarco, A.; Peluso, G. Smart Nanocomposite Hydrogels as Next-Generation Therapeutic and Diagnostic Solutions. *Gels* **2024**, *10*.

[11] Luo, Y.; Zhang, H.; Wang, Z.; Jiao, J.; Wang, Y.; Jiang, W.; Yu, T.; Liu, H.; Guan, L.; Li, M.; Wu, M. Strategic incorporation of metal ions in bone regenerative scaffolds: multifunctional platforms for advancing osteogenesis. *Regen. Biomater.* **2025**, *12*, f68.

[12] Zhao, T.; Chen, L.; Yu, C.; He, G.; Lin, H.; Sang, H.; Chen, Z.; Hong, Y.; Sui, W.; Zhao, J. Effect of injectable calcium alginate-amelogenin hydrogel on macrophage polarization and promotion of jawbone osteogenesis. *RSC Adv.* **2024**, *14*, 2016-2026.

[13] Li, Y.; Yang, G.; Wang, Y.; Li, Y.; Zhang, S.; Li, R.; Yang, L.; Wang, J.; Pei, X.; Wan, Q.; Chen, J. Osteoimmunity-regulating nanosilicate-reinforced hydrogels for enhancing osseointegration. *J. Mat. Chem. B* **2023**, *11*, 9933-9949.

[14] Ji, X.; Shao, H.; Li, X.; Ullah, M. W.; Luo, G.; Xu, Z.; Ma, L.; He, X.; Lei, Z.; Li, Q.; Jiang, X.; Yang, G.; Zhang, Y. Injectable immunomodulation-based porous chitosan microspheres/HPCH hydrogel composites as a controlled drug delivery system for osteochondral regeneration. *Biomaterials* **2022**, *285*, 121530.

[15] Qu, Y.; Wang, B.; Chu, B.; Liu, C.; Rong, X.; Chen, H.; Peng, J.; Qian, Z. Injectable and Thermosensitive Hydrogel and PDLLA Electrospun Nanofiber Membrane Composites for Guided Spinal Fusion. *ACS Appl. Mater. Interfaces* **2018**, *10*, 4462-4470.

[16] Abedi, F.; Davaran, S.; Hekmati, M.; Akbarzadeh, A.; Baradaran, B.; Moghaddam, S. V. An improved method in fabrication of smart dual-responsive nanogels for controlled release of doxorubicin and curcumin in HT-29 colon cancer cells. *J. Nanobiotechnology* **2021**, *19*, 18.

[17] Agnihotri, P.; Dheer, D.; Sangwan, A.; Chandran, V. C.; Mavlankar, N. A.; Hooda, G.; Patra, D.; Pal, A. Design of multi-responsive and actuating microgels toward on-demand drug release. *Nanoscale* **2024**, *16*, 19254-19265.

[18] Zhang, T.; Ouyang, H.; Liu, S.; Xiong, L.; Zhong, Z.; Wang, Q.; Qiu, Z.; Ding, Y.; Zhou, W.; Wang, X. pH/Thermosensitive dual-responsive hydrogel based sequential delivery for site-specific acute limb ischemia treatment. *J. Mat. Chem. B* **2022**, *10*, 7836-7846.

[19] Kaul, L.; Abdo, A. I.; Coenye, T.; Krom, B. P.; Hoogenkamp, M. A.; Zannettino, A. C. W.; Suss, R.; Richter, K. The combination of diethyldithiocarbamate and copper ions is active against Staphylococcus aureus and Staphylococcus epidermidis biofilms in vitro and in vivo. *Front. Microbiol.* **2022**, *13*, 999893.

[20] Bilal, H.; Zhang, C.; Choudhary, M. I.; Dej-Adisai, S.; Liu, Y.; Chen, Z. Copper(II) carboxylate complexes inhibit Staphylococcus aureus biofilm formation by targeting extracellular proteins. *J. Inorg. Biochem.* **2025**, *266*, 112835.

[21] Davan, I.; Fakurazi, S.; Alias, E.; Ibrahim, N.; Hwei, N. M.; Hassan, H. Astaxanthin as a Potent Antioxidant for Promoting Bone Health: An Up-to-Date Review. *Antioxidants* **2023**, *12*.

[22] Yang, G.; Liu, X.; Jing, X.; Wang, J.; Wang, H.; Chen, F.; Wang, W.; Shao, Y.; Cui, X. Astaxanthin suppresses oxidative stress and calcification in vertebral cartilage endplate via activating Nrf-2/HO-1 signaling pathway. *Int. Immunopharmacol.* **2023**, *119*, 110159.

[23] Liang, J.; Zheng, Y.; Guo, A.; Yu, H.; Xia, C.; Zhang, Z.; Wu, L.; Yan, H. Astaxanthin promotes nerve repair by regulating the M1/M2 ratio of microglia and promoting angiogenesis. *J. Funct. Foods* **2024**, *121*, 106424.

[24] Schlundt, C.; El, K. T.; Serra, A.; Dienelt, A.; Wendler, S.; Schell, H.; van Rooijen, N.; Radbruch, A.; Lucius, R.; Hartmann, S.; Duda, G. N.; Schmidt-Bleek, K. Macrophages in bone fracture healing: Their essential role in endochondral ossification. *Bone* **2018**, *106*, 78-89.

[25] Xu, D.; Zhu, W.; Ding, C.; Mei, J.; Zhou, J.; Cheng, T.; Guo, G.; Zhang, X. Self-Homeostasis Immunoregulatory Strategy for Implant-Related Infections through Remodeling Redox Balance. *ACS Nano* **2023**, *17*, 4574-4590.

[26] Diez-Tercero, L.; Delgado, L. M.; Perez, R. A. Modulation of Macrophage Response by Copper and Magnesium Ions in Combination with Low Concentrations of Dexamethasone. *Biomedicines* **2022**, *10*.

[27] Diez-Tercero, L.; Delgado, L. M.; Bosch-Rue, E.; Perez, R. A. Evaluation of the immunomodulatory effects of cobalt, copper and magnesium ions in a pro inflammatory environment. *Sci. Rep.* **2021**, *11*, 11707.

[28] Guan, X.; Wu, S.; Ouyang, S.; Ren, S.; Cui, N.; Wu, X.; Xiang, D.; Chen, W.; Yu, B.; Zhao, P.; Wang, B. Remodeling Microenvironment for Implant-Associated Osteomyelitis by Dual Metal Peroxide. *Adv. Healthc. Mater.* **2024**, *13*, e2303529.

[29] Huang, L.; Guo, Z.; Yang, X.; Zhang, Y.; Liang, Y.; Chen, X.; Qiu, X.; Chen, X. Advancements in GelMA bioactive hydrogels: Strategies for infection control and bone tissue regeneration. *Theranostics* **2025**, *15*, 460-493.

[30] Alvarez, E.; Estevez, M.; Jimenez-Jimenez, C.; Colilla, M.; Izquierdo-Barba, I.; Gonzalez, B.; Vallet-Regi, M. A versatile multicomponent mesoporous silica nanosystem with dual antimicrobial and osteogenic effects. *Acta Biomater.* **2021**, *136*, 570-581.

[31] Peng, X.; Pan, Q.; Zhang, B.; Wan, S.; Li, S.; Luo, K.; Pu, Y.; He, B. Highly Stable, Coordinated Polymeric Nanoparticles Loading Copper(II) Diethyldithiocarbamate for Combinational Chemo/Chemodynamic Therapy of Cancer. *Biomacromolecules* **2019**, *20*, 2372-2383.

[32] Ge, R.; Lin, M.; Li, X.; Liu, S.; Wang, W.; Li, S.; Zhang, X.; Liu, Y.; Liu, L.; Shi, F.; Sun, H.; Zhang, H.; Yang, B. Cu(2+)-Loaded Polydopamine Nanoparticles for Magnetic Resonance Imaging-Guided pH- and Near-Infrared-Light-Stimulated Thermochemotherapy. *ACS Appl. Mater. Interfaces* **2017**, *9*, 19706-19716.

[33] Motasadizadeh, H.; Tavakoli, M.; Damoogh, S.; Mottaghitalab, F.; Gholami, M.; Atyabi, F.; Farokhi, M.; Dinarvand, R. Dual drug delivery system of teicoplanin and phenamil based on pH-sensitive silk fibroin/sodium alginate hydrogel scaffold for treating chronic bone infection. *Biomater Adv* **2022**, *139*, 213032.

[34] Rodrigues, M. A.; Ferreira, C.; Borges, J. P.; Bernardes, B. G.; Oliveira, A. L.; Santos, J. D.; Lopes, M. A. Dual and sequential drug delivery systems with antimicrobial and bone regenerative therapeutic effects. *J. Mat. Chem. B* **2025**, *13*, 9166-9181.

[35] Zhou, R.; Ni, H.; Peng, J.; Liu, N.; Chen, S.; Shao, J.; Fu, Q.; Liu, J.; Chen, F.; Qian, Q. The mineralization, drug release and in vivo bone defect repair properties of calcium phosphates/PLA modified tantalum scaffolds. *RSC Adv.* **2020**, *10*, 7708-7717.

[36] Tiwari, A.; Haj, N.; Elgrably, B.; Berihu, M.; Laskov, V.; Barash, S.; Zigron, S.; Sason, H.; Shamay, Y.; Karni-Ashkenazi, S.; Holdengreber, M.; Saar, G.; Vandoorne, K. Cross-Modal Imaging Reveals Nanoparticle Uptake Dynamics in Hematopoietic Bone Marrow during Inflammation. *ACS Nano* **2024**, *18*, 7098-7113.

[37] Makabenta, J.; Nabawy, A.; Chattopadhyay, A. N.; Jeon, T.; Park, J.; Lo, P. C.; Nosovitski, S.; Huang, R.; Li, C. H.; Jiang, M.; Rotello, V. M. Antimicrobial polymer-loaded hydrogels for the topical treatment of multidrug-resistant wound biofilm infections. *J. Control. Release* **2023**, *362*, 513-523.

[38] Xu, Y.; Luo, Y.; Weng, Z.; Xu, H.; Zhang, W.; Li, Q.; Liu, H.; Liu, L.; Wang, Y.; Liu, X.; Liao, L.; Wang, X. Microenvironment-Responsive Metal-Phenolic Nanozyme Release Platform with Antibacterial, ROS Scavenging, and Osteogenesis for Periodontitis. *ACS Nano* **2023**, *17*, 18732-18746.

[39] Qiu, Y.; Park, K. Environment-sensitive hydrogels for drug delivery. *Adv. Drug Deliv. Rev.* **2001**, *53*, 321-339.

[40] Gao, K.; Xu, K. Advancements and Prospects of pH-Responsive Hydrogels in Biomedicine. *Gels* **2025**, *11*.

[41] Peppas, N. A.; Bures, P.; Leobandung, W.; Ichikawa, H. Hydrogels in pharmaceutical formulations. *Eur. J. Pharm. Biopharm.* **2000**, *50*, 27-46.

[42] Thang, N. H.; Chien, T. B.; Cuong, D. X. Polymer-Based Hydrogels Applied in Drug Delivery: An Overview. *Gels* **2023**, *9*.

[43] Lister, J. L.; Horswill, A. R. Staphylococcus aureus biofilms: recent developments in biofilm dispersal. *Front. Cell. Infect.*

Microbiol. **2014**, *4*, 178.
[44] Li, J.; Mooney, D. J. Designing hydrogels for controlled drug delivery. *Nat. Rev. Mater.* **2016**, *1*.
[45] Huh, A. J.; Kwon, Y. J. "Nanoantibiotics": a new paradigm for treating infectious diseases using nanomaterials in the antibiotics resistant era. *J. Control. Release* **2011**, *156*, 128-145.
[46] Shi, W.; Li, T.; Guo, X.; Jiang, X. Thermosensitive hydroxypropyl chitin-based microneedle patch for long-term management of neuropathic pain. *Carbohydr. Polym.* **2026**, *373*, 124596.
[47] Li, T.; Huang, L.; Jiang, X. Visualization of thermosensitive hydroxypropyl chitin with aggregation-induced emission features for sustained-release drug delivery. *Int. J. Biol. Macromol.* **2025**, *331*, 148418.
[48] Abdullah, Z.; Ashraf, M. U.; Barkat, K.; Badshah, S. F.; Rehman, U.; Razzaq, A.; Mahmood, A.; Ulhaq, F.; Chopra, H.; Rashid, S.; Valko, M.; Alomar, S.; Kuca, K.; Sharma, R. Formulation of pH-responsive highly swellable hydrogel scaffolds for controlled release of tramadol HCl: characterization and biocompatibility evaluation. *Front. Bioeng. Biotechnol.* **2023**, *11*, 1190322.
[49] Visan, A. I.; Negut, I. Development and Applications of PLGA Hydrogels for Sustained Delivery of Therapeutic Agents. *Gels (Basel, Switzerland)* **2024**, *10*, 497.
[50] Wu, X. X.; Zhang, Y.; Hu, T.; Li, W. X.; Li, Z. L.; Hu, H. J.; Zhu, S. R.; Chen, W. Z.; Zhou, C. S.; Jiang, G. B. Long-term antibacterial composite via alginate aerogel sustained release of antibiotics and Cu used for bone tissue bacteria infection. *Int. J. Biol. Macromol.* **2021**, *167*, 1211-1220.
[51] Zhang, J.; Xue, S.; Zhu, X.; Zhao, Y.; Chen, Y.; Tong, J.; Shi, X.; Du Y; Zhong, Z.; Ye, Q. Emerging chitin nanogels/rectorite nanocomposites for safe and effective hemorrhage control. *J. Mat. Chem. B* **2019**, *7*, 5096-5103.
[52] Dai, T.; Wang, C.; Wang, Y.; Xu, W.; Hu, J.; Cheng, Y. A Nanocomposite Hydrogel with Potent and Broad-Spectrum Antibacterial Activity. *ACS Appl. Mater. Interfaces* **2018**, *10*, 15163-15173.
[53] Petronglo, J. R.; Eichelberger, K. R.; Cassat, J. Osteoclast differentiation alters monocyte inflammatory responses to Staphylococcus aureus. *The Journal of immunology (1950)* **2022**, *208*, 164.
[54] Askarian, F.; Wagner, T.; Johannessen, M.; Nizet, V. Staphylococcus aureus modulation of innate immune responses through Toll-like (TLR), (NOD)-like (NLR) and C-type lectin (CLR) receptors. *FEMS Microbiol. Rev.* **2018**, *42*, 656-671.
[55] de Souza, A. P.; Vale, V. L.; Silva, M. C.; Araujo, I. B.; Trindade, S. C.; de Moura-Costa, L. F.; Rodrigues, G. C.; Sales, T. S.; Dos, S. H.; de Carvalho-Filho, P. C.; de Oliveira-Neto, M. G.; Schaer, R. E.; Meyer, R. MAPK involvement in cytokine production in response to Corynebacterium pseudotuberculosis infection. *BMC Microbiol.* **2014**, *14*, 230.
[56] Cerdeira, C. D.; Brigagao, M. Targeting Macrophage Polarization in Infectious Diseases: M1/M2 Functional Profiles, Immune Signaling and Microbial Virulence Factors. *Immunol. Invest.* **2024**, *53*, 1030-1091.
[57] Pluddemann, A.; Mukhopadhyay, S.; Gordon, S. The interaction of macrophage receptors with bacterial ligands. *Expert Rev. Mol. Med.* **2006**, *8*, 1-25.
[58] Massaccesi, L.; Galliera, E.; Pellegrini, A.; Banfi, G.; Corsi, R. M. Osteomyelitis, Oxidative Stress and Related Biomarkers. *Antioxidants* **2022**, *11*.
[59] Cinelli, M. A.; Do, H. T.; Miley, G. P.; Silverman, R. B. Inducible nitric oxide synthase: Regulation, structure, and inhibition. *Med. Res. Rev.* **2020**, *40*, 158-189.
[60] Souza, P. P. C.; Lerner, U. H. The role of cytokines in inflammatory bone loss. *Immunol. Invest.* **2013**, *42*, 555-622.
[61] Lampiasi, N.; Russo, R.; Zito, F. The Alternative Faces of Macrophage Generate Osteoclasts. *Biomed Res. Int.* **2016**, *2016*, 9089610.
[62] Romero-Gavilan, F.; Cerqueira, A.; Garcia-Arnaez, I.; Scalschi, L.; Vicedo, B.; Azkargorta, M.; Elortza, F.; Izquierdo, R.; Gurruchaga, M.; Goni, I.; Suay, J. Proteomic evaluation of borosilicate hybrid sol-gel coatings with osteogenic, immunomodulatory and antibacterial properties. *Colloid Surf. B-Biointerfaces* **2025**, *250*, 114561.
[63] Vasconcelos, D. M.; Santos, S. G.; Lamghari, M.; Barbosa, M. A. The two faces of metal ions: From implants rejection to tissue repair/regeneration. *Biomaterials* **2016**, *84*, 262-275.
[64] Godoy-Gallardo, M.; Eckhard, U.; Delgado, L. M.; de Roo Puente, Y. J. D.; Hoyos-Nogues, M.; Gil, F. J.; Perez, R. A. Antibacterial approaches in tissue engineering using metal ions and nanoparticles: From mechanisms to applications. *Bioact. Mater.* **2021**, *6*, 4470-4490.
[65] Li, H.; Yuan, Y.; Zhang, L.; Xu, C.; Xu, H.; Chen, Z. Reprogramming Macrophage Polarization, Depleting ROS by Astaxanthin and Thioketal-Containing Polymers Delivering Rapamycin for Osteoarthritis Treatment. *Adv. Sci.* **2024**, *11*, e2305363.
[66] Takeuchi, O.; Kaufmann, A.; Grote, K.; Kawai, T.; Hoshino, K.; Morr, M.; Mühlradt, P. F.; Akira, S. Cutting edge: preferentially the R-stereoisomer of the mycoplasmal lipopeptide macrophage-activating lipopeptide-2 activates immune cells through a toll-like receptor 2- and MyD88-dependent signaling pathway. *Journal of immunology (Baltimore, Md. : 1950)* **2000**, *164*, 554-557.
[67] Schwandner, R.; Dziarski, R.; Wesche, H.; Rothe, M.; Kirschning, C. J. Peptidoglycan- and lipoteichoic acid-induced cell activation is mediated by toll-like receptor 2. *The Journal of biological chemistry* **1999**, *274*, 17406-17409.
[68] Guilliams, M.; Thierry, G. R.; Bonnardel, J.; Bajenoff, M. Establishment and Maintenance of the Macrophage Niche. *Immunity* **2020**, *52*, 434-451.
[69] Marriott, I.; Gray, D. L.; Tranguch, S. L.; Fowler, V. G. J.; Stryjewski, M.; Scott Levin, L.; Hudson, M. C.; Bost, K. L. Osteoblasts express the inflammatory cytokine interleukin-6 in a murine model of Staphylococcus aureus osteomyelitis and infected human bone tissue. *The American journal of pathology* **2004**, *164*, 1399-1406.
[70] Bost, K. L.; Ramp, W. K.; Nicholson, N. C.; Bento, J. L.; Marriott, I.; Hudson, M. C. Staphylococcus aureus infection of mouse or human osteoblasts induces high levels of interleukin-6 and interleukin-12 production. *The Journal of infectious diseases* **1999**, *180*, 1912-1920.
[71] Blair, H. C.; Larrouture, Q. C.; Li, Y.; Lin, H.; Beer-Stoltz, D.; Liu, L.; Tuan, R. S.; Robinson, L. J.; Schlesinger, P. H.; Nelson, D. J. Osteoblast Differentiation and Bone Matrix Formation In Vivo and In Vitro. *Tissue engineering. Part B, Reviews* **2017**, *23*, 268-280.
[72] Griffanti, G.; McKee, M. D.; Nazhat, S. N. Mineralization of Bone Extracellular Matrix-like Scaffolds Fabricated as Silk Sericin-Functionalized Dense Collagen-Fibrin Hybrid Hydrogels. *Pharmaceutics* **2023**, *15*, 1087.
[73] Chan, W. C. W.; Tan, Z.; To, M. K. T.; Chan, D. Regulation and Role of Transcription Factors in Osteogenesis. *Int. J. Mol. Sci.* **2021**, *22*, 5445.
[74] Carvalho, M. S.; Poundarik, A. A.; Cabral, J. M. S.; Da Silva, C. L.; Vashishth, D. Biomimetic matrices for rapidly forming mineralized bone tissue based on stem cell-mediated osteogenesis. *Sci. Rep.* **2018**, *8*, 14388.
[75] Bailey, S.; Karsenty, G.; Gundberg, C.; Vashishth, D. Osteocalcin and osteopontin influence bone morphology and mechanical properties. *Ann. N. Y. Acad. Sci.* **2017**, *1409*, 79-84.
[76] Johansen, L. K.; Frees, D.; Aalbaek, B.; Koch, J.; Iburg, T.; Nielsen, O. L.; Leifsson, P. S.; Jensen, H. E. A porcine model of acute, haematogenous, localized osteomyelitis due to Staphylococcus aureus: a pathomorphological study. *APMIS.* **2011**, *119*, 111-118.
[77] Mandell, J. C.; Khurana, B.; Smith, J. T.; Czuczman, G. J.; Ghazikhanian, V.; Smith, S. E. Osteomyelitis of the lower extremity: pathophysiology, imaging, and classification, with an emphasis on diabetic foot infection. *Emerg. Radiol.* **2018**, *25*, 175-188.
[78] Baertl, S.; Gens, L.; Nehrbass, D.; Sumrall, E. T.; Zeiter, S.; Mannala, G. K.; Rupp, M.; Walter, N.; Richards, R. G.; Moriarty, T. F.; Alt, V. Staphylococcus aureus From an Acute Fracture-related Infection Displays Important Bacteriological and Histopathologic Differences From a Chronic Equivalent in a Murine Bone Infection Model. *Clin. Orthop. Relat. Res.* **2023**, *481*, 2044-2060.
[79] Margaroli, C.; Horati, H.; Garratt, L. W.; Giacalone, V. D.; Schofield, C.; Dittrich, A. S.; Rosenow, T.; Dobosh, B. S.; Lim, H. S.; Frey, D. L.; Veltman, M.; Silva, G. L.; Brown, M. R.; Schultz, C.; Tiddens, H. A. W. M.; Ranganathan, S.; Chandler, J. D.; Qiu, P.; Peng, L.; Scholte, B. J.; Mall, M. A.; Kicic, A.; Guglani, L.; Stick, S. M.; Janssens, H. M.; Tirouvanziam, R. Macrophage PD-1 associates with neutrophilia and reduced bacterial killing in early cystic fibrosis airway disease. *J. Cyst. Fibros* **2022**, *21*, 967-976.

[80] Surendar, J.; Hackenberg, R. K.; Schmitt-Sanchez, F.; Ossendorff, R.; Welle, K.; Stoffel-Wagner, B.; Sage, P. T.; Burger, C.; Wirtz, D. C.; Strauss, A. C.; Schildberg, F. A. Osteomyelitis is associated with increased anti-inflammatory response and immune exhaustion. *Front. Immunol.* **2024**, *15*, 1396592.

[81] Huang, X.; Venet, F.; Wang, Y. L.; Lepape, A.; Yuan, Z.; Chen, Y.; Swan, R.; Kherouf, H.; Monneret, G.; Chung, C.; Ayala, A. PD-1 expression by macrophages plays a pathologic role in altering microbial clearance and the innate inflammatory response to sepsis. *Proc. Natl. Acad. Sci. U. S. A.* **2009**, *106*, 6303-6308.

[82] Lee, S. I.; Kim, N. Y.; Chung, C.; Park, D.; Kang, D. H.; Kim, D. K.; Yeo, M.; Sun, P.; Lee, J. E. IL-6 and PD-1 antibody blockade combination therapy regulate inflammation and T lymphocyte apoptosis in murine model of sepsis. *BMC Immunol.* **2025**, *26*, 3.

[83] Masters, E. A.; Ricciardi, B. F.; Bentley, K. L. D. M.; Moriarty, T. F.; Schwarz, E. M.; Muthukrishnan, G. Skeletal infections: microbial pathogenesis, immunity and clinical management. *Nat. Rev. Microbiol.* **2022**, *20*, 385-400.

[84] Lin, Y.; Su, J.; Wang, Y.; Xu, D.; Zhang, X.; Yu, B. mRNA Transcriptome Analysis of Bone in a Mouse Model of Implant-Associated Staphylococcus aureus Osteomyelitis. *Infect. Immun.* **2021**, *89*.

[85] York, B.; Cha, J.; Dao, A.; Gane, S.; Policinski, I.; Rahman, M. Diagnosis: chronic osteomyelitis. *Eplasty* **2014**, *14*, c8.

[86] Ikpeme, I. A.; Ngim, N. E.; Ikpeme, A. A. Diagnosis and treatment of pyogenic bone infections. *Afr. Health Sci.* **2010**, *10*, 82-88.

[87] Qadri, S.; Haik, Y.; Mensah-Brown, E.; Bashir, G.; Fernandez-Cabezudo, M. J.; Al-Ramadi, B. K. Metallic nanoparticles to eradicate bacterial bone infection. *Nanomedicine* **2017**, *13*, 2241-2250.

[88] Yang, Y.; Li, M.; Zhou, B.; Jiang, X.; Zhang, D.; Luo, H. Graphene oxide/gallium nanoderivative as a multifunctional modulator of osteoblastogenesis and osteoclastogenesis for the synergistic therapy of implant-related bone infection. *Bioact. Mater.* **2023**, *25*, 594-614.

[89] Yang, Y.; Li, M.; Luo, H.; Zhang, D. Surface-Decorated Graphene Oxide Sheets with Copper Nanoderivatives for Bone Regeneration: An In Vitro and In Vivo Study Regarding Molecular Mechanisms, Osteogenesis, and Anti-infection Potential. *ACS Infect. Dis.* **2022**, *8*, 499-515.

[90] van Vugt, T. A. G.; Arts, J. J.; Geurts, J. A. P. Antibiotic-Loaded Polymethylmethacrylate Beads and Spacers in Treatment of Orthopedic Infections and the Role of Biofilm Formation. *Front. Microbiol.* **2019**, *10*, 1626.

[91] Smith, M.; Roberts, M.; Al-Kassas, R. Implantable drug delivery systems for the treatment of osteomyelitis. *Drug Dev. Ind. Pharm.* **2022**, *48*, 511-527.

[92] Wang, K.; Jiang, K.; Luo, C.; You, X.; Shen, H.; Wu, D.; Huang, F.; Li, L.; Huang, S.; Xu, J.; Li, Z. An osteoimmunomodulatory Ca2+/Zn2+-doped scaffold promotes M2 macrophage polarization via the src-mediated chemoking signaling pathway to enhance osteoinduction. *Composites. Part B, Engineering* **2024**, *284*, 111653.

[93] Bessa-Gonçalves, M.; Ribeiro-Machado, C.; Costa, M.; Ribeiro, C. C.; Barbosa, J. N.; Barbosa, M. A.; Santos, S. G. Magnesium incorporation in fibrinogen scaffolds promotes macrophage polarization towards M2 phenotype. *Acta Biomater.* **2023**, *155*, 667-683.

[94] Lu, H.; Liu, Y.; Guo, J.; Wu, H.; Wang, J.; Wu, G. Biomaterials with Antibacterial and Osteoinductive Properties to Repair Infected Bone Defects. *Int. J. Mol. Sci.* **2016**, *17*, 334.

[95] Chen, B.; Liang, Y.; Zhang, J.; Bai, L.; Xu, M.; Han, Q.; Han, X.; Xiu, J.; Li, M.; Zhou, X.; Guo, B.; Yin, Z. Synergistic enhancement of tendon-to-bone healing via anti-inflammatory and pro-differentiation effects caused by sustained release of Mg(2+)/curcumin from injectable self-healing hydrogels. *Theranostics* **2021**, *11*, 5911-5925.

[96] Kapusta, O.; Jarosz, A.; Stadnik, K.; Giannakoudakis, D. A.; Barczyński, B.; Barczak, M. Antimicrobial Natural Hydrogels in Biomedicine: Properties, Applications, and Challenges-A Concise Review. *Int. J. Mol. Sci.* **2023**, *24*, 2191.

[97] Dai, C.; Lin, J.; Li, H.; Shen, Z.; Wang, Y.; Velkov, T.; Shen, J. The Natural Product Curcumin as an Antibacterial Agent: Current Achievements and Problems. *Antioxidants (Basel, Switzerland)* **2022**, *11*, 459.

[98] Ghosh, S.; Ghosh, S.; Yeung, K. W. K.; Xu, C.; Wu, J.; Mao, C.; Ling, Z.; Okuro, K.; Qiao, W. Dual-responsive copper complex delivered by dissolvable microneedle promotes polymicrobial infection eradication and cutaneous wound healing. *Materials today. Bio* **2025**, *34*, 102219.

[99] Baino, F. Copper-doped Ordered Mesoporous Bioactive Glass: A Promising Multifunctional Platform for Bone Tissue Engineering (†). *Bioengineering (Basel, Switzerland)* **2020**, *7*, 45.

[100] Liu, Y.; Wang, G.; Luo, H.; Zhao, B.; Liao, M.; Dai, Q.; Li, M.; Li, Q.; Cao, X. Phosphoserine enhanced Cu-doped bioactive glass dynamic dual-network hydrogel for craniofacial bone defect repair. *Regen. Biomater.* **2023**, *10*, d54.

[101] Feng, S.; Peng, X.; Wei, X.; Deng, Y.; Pu, X.; Gao, X.; Yu, X. Ligand-dependent activity engineering of Cu-MOFs based on biomimetic strategies for nanozyme-decorated smart hydrogels for therapy of inflammatory bone defects. *Journal of materials chemistry. B* **2025**, *13*, 12448-12468.

[102] Pacifici, N.; Bolandparvaz, A.; Lewis, J. S. Stimuli-Responsive Biomaterials for Vaccines and Immunotherapeutic Applications. *Adv. Therap.* **2020**, *3*, 2000129.

[103] Bailey, S.; Karsenty, G.; Gundberg, C.; Vashishth, D. Osteocalcin and osteopontin influence bone morphology and mechanical properties. *Ann. N. Y. Acad. Sci.* **2017**, *1409*, 79-84.

[104] Thurner, P. J.; Chen, C. G.; Ionova-Martin, S.; Sun, L.; Harman, A.; Porter, A.; Ager, J. W. R.; Ritchie, R. O.; Alliston, T. Osteopontin deficiency increases bone fragility but preserves bone mass. *Bone* **2010**, *46*, 1564-1573.

[105] Liu, H.; Liu, J.; Qi, C.; Fang, Y.; Zhang, L.; Zhuo, R.; Jiang, X. Thermosensitive injectable in-situ forming carboxymethyl chitin hydrogel for three-dimensional cell culture. *Acta Biomater.* **2016**, *35*, 228-237.

[106] Combes, A.; Rieb, C.; Haye, L.; Klymchenko, A. S.; Serra, C. A.; Reisch, A. Mixing versus Polymer Chemistry in the Synthesis of Loaded Polymer Nanoparticles through Nanoprecipitation. *Langmuir* **2023**, *39*, 16532-16542.

[107] Lim, S. H.; Wong, T. W.; Tay, W. X. Overcoming colloidal nanoparticle aggregation in biological milieu for cancer therapeutic delivery: Perspectives of materials and particle design. *Adv. Colloid. Interface. Sci.* **2024**, *325*, 103094.

[108] Mehta, P.; Shende, P. Evasion of opsonization of macromolecules using novel surface-modification and biological-camouflage-mediated techniques for next-generation drug delivery. *Cell. Biochem. Funct.* **2023**, *41*, 1031-1043.

[109] Lamprea Pineda, P. A.; Demeestere, K.; Toledo, M.; Boon, N.; Van Langenhove, H.; Walgraeve, C. Long-term biofiltration of gaseous N,N-dimethylformamide: Operational performance and microbial diversity analysis at different conditions. *J. Hazard. Mater.* **2023**, *447*, 130767.

[110] Bao, Q.; Fu, K.; Ren, Q.; Zhong, Y.; Qian, D. Accuracy Profiles for Analyzing Residual Solvents in Textiles by GC-MS. *J. Chromatogr. Sci.* **2017**, *55*, 882-890.

[111] Clay, N. E.; Whittenberg, J. J.; Leong, J.; Kumar, V.; Chen, J.; Choi, I.; Liamas, E.; Schieferstein, J. M.; Jeong, J. H.; Kim, D. H.; Zhang, Z. J.; Kenis, P. J. A.; Kim, I. W.; Kong, H. Chemical and mechanical modulation of polymeric micelle assembly. *Nanoscale* **2017**, *9*, 5194-5204.

[112] Hristov, D. R.; Mahon, E.; Dawson, K. A. Controlling aqueous silica nanoparticle synthesis in the 10-100 nm range. *Chem. Commun.* **2015**, *51*, 17420-17423.

[113] Trotsiuk, L.; Antanovich, A.; Lizunova, A.; Kulakovich, O. Direct synthesis of amphiphilic polyvinylpyrrolidone-capped gold nanoparticles in chloroform. *Colloid Interface Sci. Commun.* **2020**, *37*, 100289.

[114] Carmona-Almazan, J. P.; Castro-Cesena, A. B.; Aguila, S. A. Evaluation of the release kinetics of hydrophilic and lipophilic compounds from lipid-polymer hybrid nanoparticles. *Nanoscale* **2024**, *16*, 15801-15814.

[115] Witzler, M.; Vermeeren, S.; Kolevatov, R. O.; Haddad, R.; Gericke, M.; Heinze, T.; Schulze, M. Evaluating Release Kinetics from Alginate Beads Coated with Polyelectrolyte Layers for Sustained Drug Delivery. *ACS Appl. Bio Mater.* **2021**, *4*, 6719-6731.

[116] Wu, H.; Lin, Y.; Lin, Y.; Deng, M.; Hou, J.; Liu, D.; Cui, Z.; Guan, D.; Wang, J.; Yu, B. Ozone-delivering nanocomposite hydrogel for acute Staphylococcus aureus osteomyelitis treatment via neutrophil regulation. *Chemical engineering journal (Lausanne, Switzerland : 1996)* **2024**, *489*, 151209.

FIGURES.

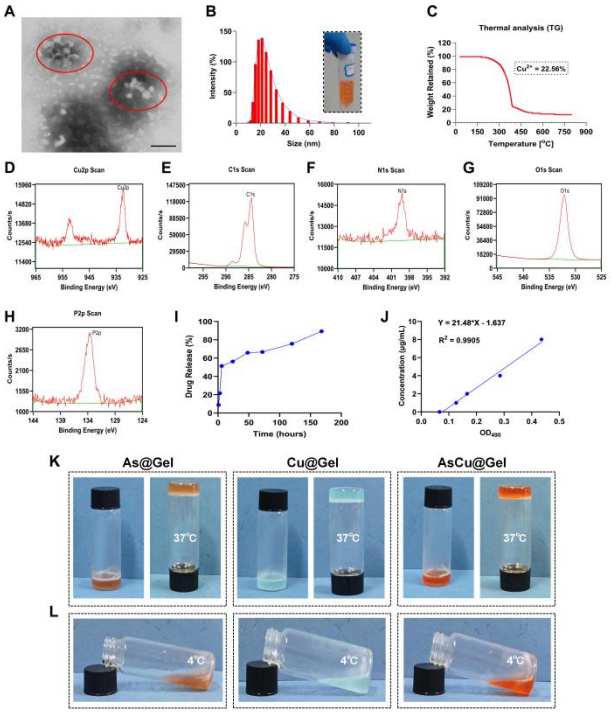

Figure 1. Characteristics of As/Cu^{2+}-loaded DSPE-PEG_{2000} nanoparticles (NPs) and gel. (A) Transmission electron microscopy (TEM) image of nanoparticles (NPs). Scale bar: 100 nm. (B) Size distribution of NPs. (C) Thermogravimetric analysis (TGA) of Cu^{2+}. (D-H) X-ray photoelectron spectroscopy (XPS) analysis for copper (Cu), carbon (C), nitrogen (N), oxygen (O), and phosphorus (P). (I) Drug release profile of AsCu@NPs. (J) Standard curve for detecting the concentration of DiI-labeled AsCu@NPs. (K) and (L) Images of As@Gel, Cu@Gel, and AsCu@Gel solutions at varying temperatures.

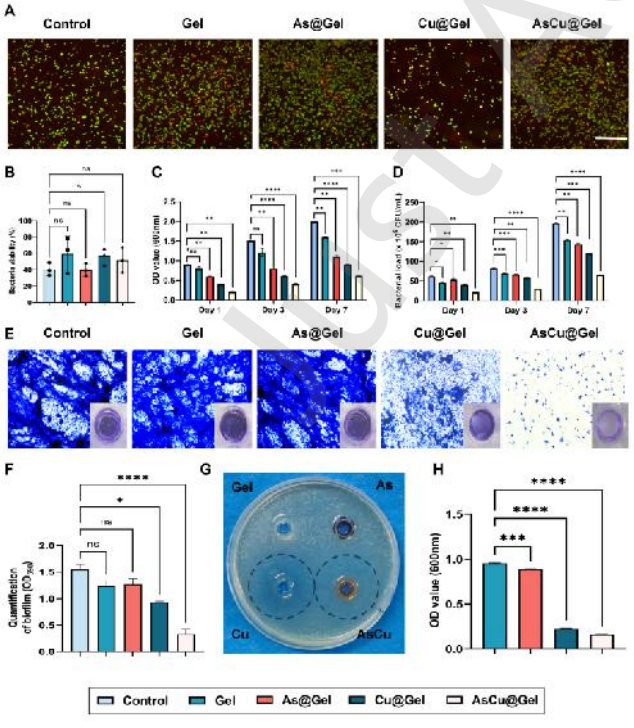

Figure 2. The antibacterial effect of AsCu@Gel *in vitro*. (A) Representative fluorescence images obtained from the Live/Dead staining assay show the viability of *S. aureus* co-cultured with nanocomposite hydrogel for 24 h. Scale bars: 100 μm. (B) The viability of *S. aureus* co-cultured with nanocomposite hydrogel for 24 h (n = 3). (C) The OD_{600} values of *S. aureus* suspension at days 1, 3, and 7 with different hydrogel material groups (n = 3). (D) Representative images of *S. aureus* treated with different hydrogel material groups in TSA at days 1, 3, and 7 (n = 3). (E) Representative images of biofilm formation of *S. aureus* treated with different hydrogel material groups. Scale bars: 100 μm. (F) The OD_{590} values of biofilm suspension with different hydrogel material groups (n = 3). (G) The size of inhibition zones of *S. aureus* treated with different hydrogel material groups and (H) quantitative analysis (OD_{600}) (n = 3). Data are expressed as mean ± SD (n = 3). ns = not significant; *p < 0.05; **p < 0.01; ***p < 0.001; ****p < 0.0001.

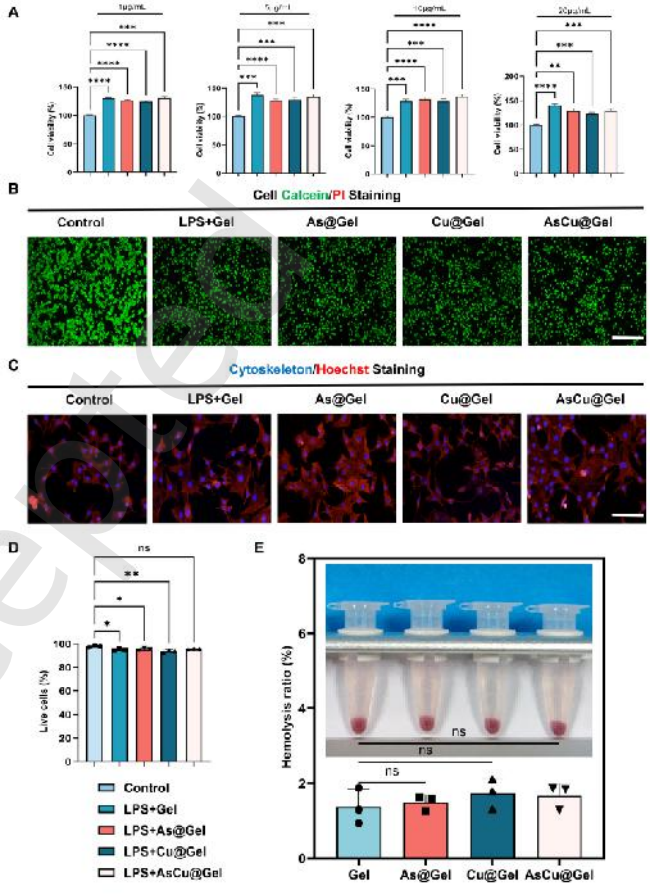

Figure 3. *In vitro* assessment of the cytotoxicity and cytocompatibility of AsCu@Gel. (A) Assessment of cell viability in the RAW264.7 cell line cultured on hydrogels across various concentrations (n = 3). (B) Live/dead staining results for the RAW264.7 cell line following 24 h of co-culture with different nanocomposite hydrogel in LPS-mediated cell models (Scale bars: 100 μm). (C) Cytoskeleton staining images of cells co-cultured with various nanocomposite hydrogel (Scale bars: 100 μm). (D) Quantitative analysis of the live/dead staining data (n = 3). (E) Hemolysis test results after 2 h of co-culture with different nanocomposite hydrogel. Quantitative analysis of the hemolysis test (n = 3). Data are expressed as mean ± SD (n = 3). ns = not significant; *p < 0.05; **p < 0.01; ***p < 0.001; ****p < 0.0001.

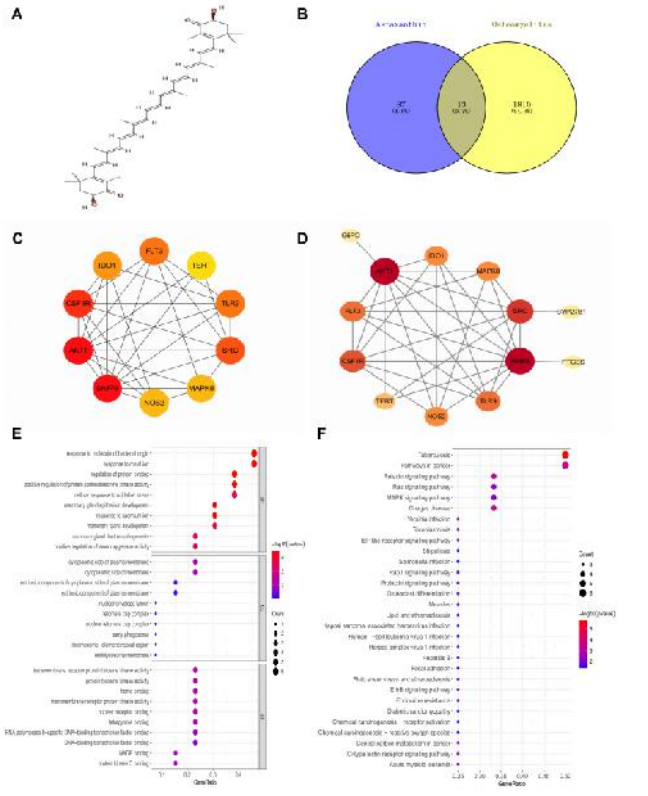

Figure 4. Network pharmacology reveals *As*'s multi-target mechanisms against acute *Staphylococcal* osteomyelitis (AOM). A) 2D molecular structure of *As*. B) Venn diagram of 100 predicted *As* targets, with 13 overlapping AOM-related targets. C) Protein-protein interaction (PPI) network of top *As*-AOM intersection targets (node size = degree centrality). D) Top 10 hub targets ranked by maximal clique centrality (MCC), highlighting core regulatory genes. E) Gene Ontology (GO) enrichment showing *As*'s biological processes (BP), cellular components (CC), and molecular functions (MF) in AOM. F) KEGG pathway analysis of *As*'s therapeutic mechanisms, with size indicating gene count and color representing p-value significance.

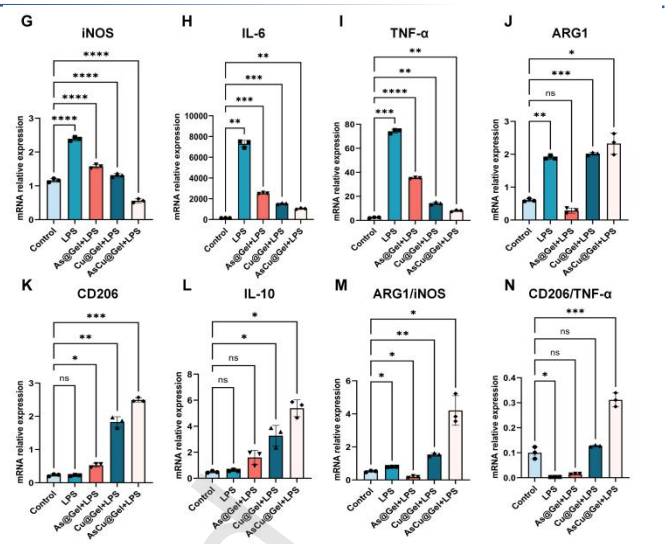

Figure 5. AsCu@Gel modulates inflammation in LPS-stimulated macrophages. (A) EdU staining of the RAW264.7 cell line after co-culture with various nanocomposite hydrogel in an LPS-mediated cellular inflammation model (Scale bars: 100 μm). (B) Detection of ROS-positive cells in the RAW264.7 cell line (Scale bars: 200 μm). (C) Flow cytometry analysis of cell apoptosis. (D) Quantitative assessment of EdU staining in the RAW264.7 cell line following co-culture with different nanocomposite hydrogel in the LPS-mediated inflammation model (n = 3). (E) Quantitative analysis of ROS fluorescence percentage in the RAW264.7 cell line (n = 3). (F) The percentage of early apoptotic cells is significantly reduced in the presence of AsCu@Gel compared to the other groups (n = 3). (G-I) Expression levels of M1 macrophage marker genes (n = 3). (J-L) Expression levels of M2 macrophage marker genes (n = 3). (M, N) Anti-/pro-inflammatory cytokines ratios (n = 3). Data are expressed as mean ± SD (n = 3). ns = not significant; *$p < 0.05$; **$p < 0.01$; ***$p < 0.001$; ****$p < 0.0001$.

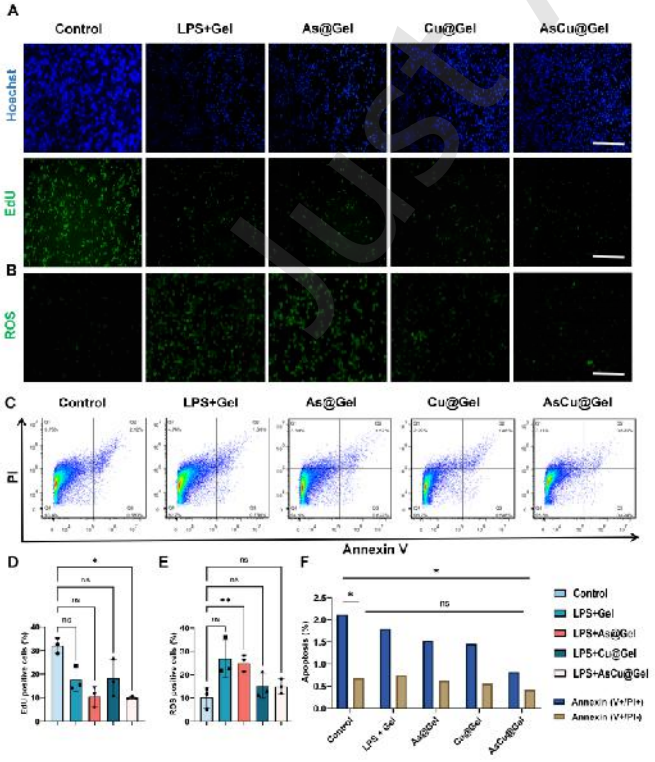

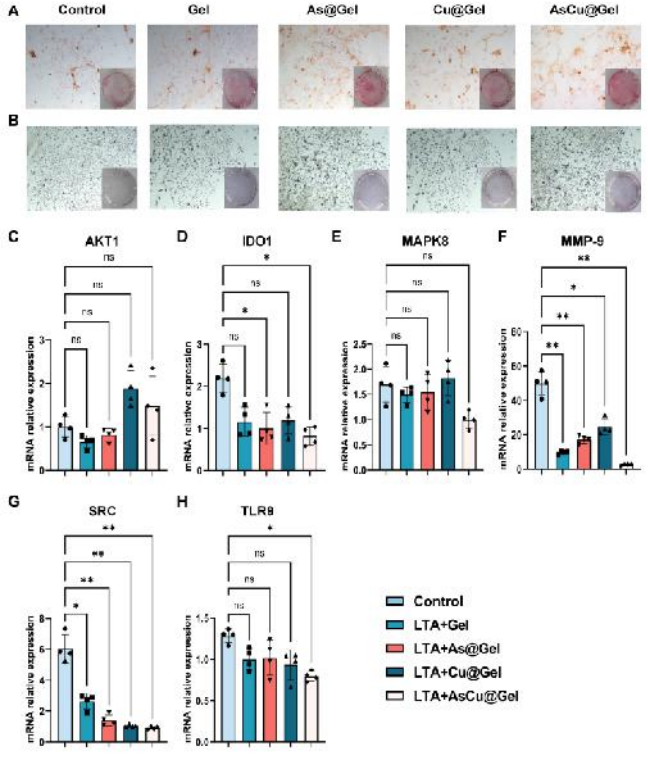

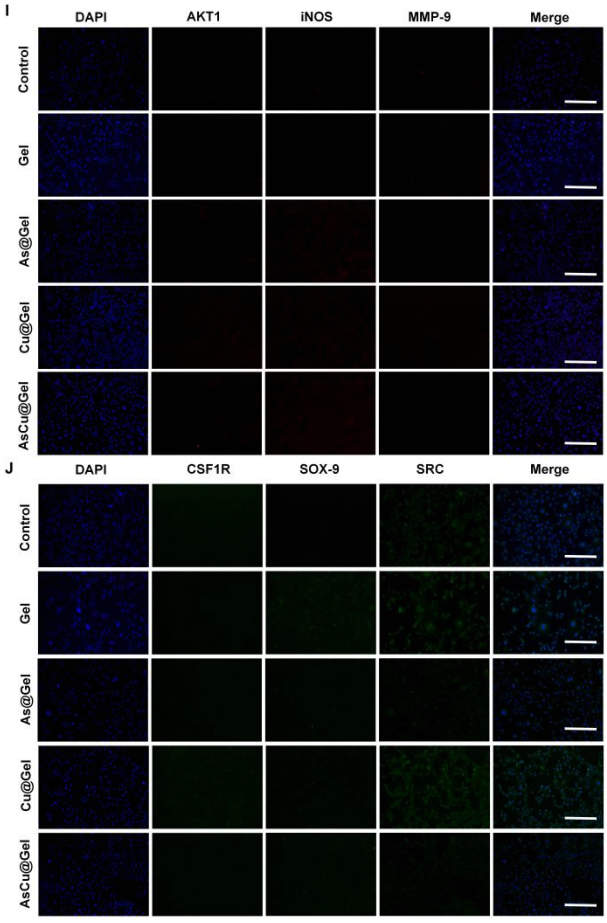

Figure 6. AsCu@Gel promotes osteogenesis and mitigates inflammatory signaling. (A) Alizarin Red staining of mineralized nodules after 7 days. (B) ALP staining (blue) of MC3T3 cells after 7 days. (C-H) qPCR analysis of osteogenic (AKT1) and inflammatory (IDO1, MAPK8, MMP-9, SRC, TLR9) genes in LTA-stimulated RAW264.7 cells (n = 4). (I-J) Immunofluorescence of osteomyelitis-associated markers (iNOS, CSF1R, AKT1) (Scale bars: 100 μm) (n = 4). Data are expressed as mean ± SD (n ≥ 3). ns = not significant; *$p < 0.05$; **$p < 0.01$.

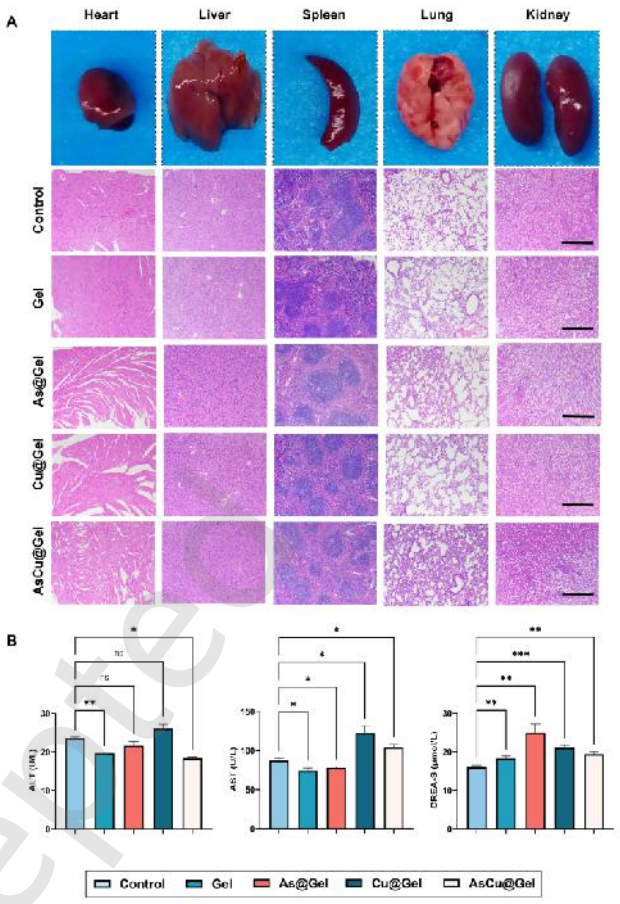

Figure 7. *In vivo* biocompatibility assessment of AsCu@Gel. (A) Histopathological staining on organ sections (heart, liver, spleen, lungs, kidneys) after 10-day implantation shows preserved tissue architecture without pathological changes (Scale bars: 100 μm). (B) Serum biochemical markers confirm hepatorenal safety. Dotted lines indicate species-specific physiological ranges (n ≥ 3). Data are expressed as mean ± SD (n ≥ 3). ns = not significant; *$p < 0.05$; **$p < 0.01$; ***$p<0.001$.

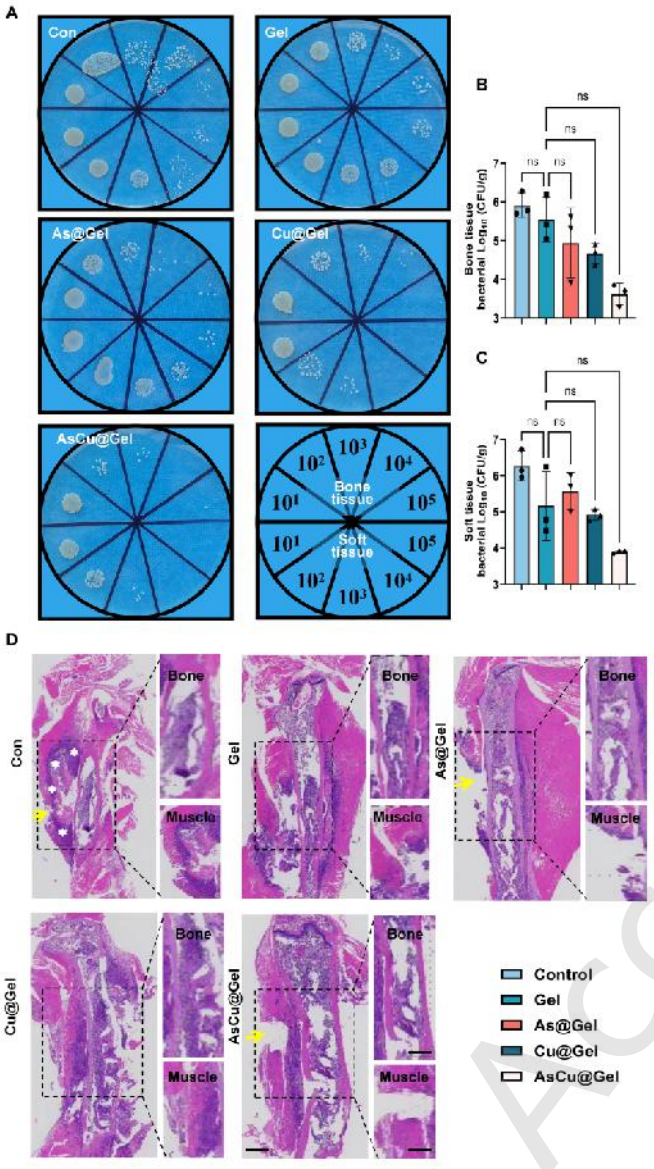

Figure 8. *In vivo* antibacterial activity of AsCu@Gel. (A) Representative images of *S. aureus* colonies from bone and muscle tissue in AOM mice treated with different hydrogels (TSA plates). (B, C) Quantitative analysis of *S. aureus* CFUs in bone (B) and muscle (C) (n = 3). (D) H&E staining of infected tissues (scale bars: left = 500 μm, top right = 100 μm, bottom = 50 μm) (n = 5). Data are expressed as mean ± SD; ns = not significant.

Electronic Supplementary Material

An injectable AsCu-nanocomposite hydrogel breaks the pathological triad of acute osteomyelitis via synergistic bactericidal and macrophage-reprogramming therapy

Vidmi Taolam Martin[1,2,§], Yanpeng Lin[3,§], Hangtian Wu[1,2,§], Bo Yu[4], Daogang Guan[5,6*] ✉, Jun Wang[7*] ✉, and Bin Yu[1,2*] ✉

[1] *Division of Orthopaedics and Traumatology, Department of Orthopaedics, Nanfang Hospital, Southern Medical University, Guangzhou 510515, China*
[2] *Guangdong Provincial Key Laboratory of Bone and Cartilage Regeneration Medicine, Nanfang Hospital, Southern Medical University, Guangzhou 510515, China*
[3] *Department of Radiology, Nanfang Hospital, Southern Medical University, Guangzhou 510515, China*
[4] *Department of Orthopaedics and Traumatology, Zhujiang Hospital, Southern Medical University, Guangzhou 510282, China*
[5] *Department of Biochemistry and Molecular Biology, School of Basic Medical Sciences, Southern Medical University, Guangzhou 510515, China*
[6] *Guangdong Provincial Key Laboratory of Single Cell Technology and Application, Southern Medical University, Guangzhou 510515, China*
[7] *School of Animal Science and Technology, Foshan University, Foshan 528231, China*
[§] *Vidmi Taolam Martin, Yanpeng Lin, and Hangtian Wu contributed equally to this work.*

✉ Address correspondence to Daogang Guan, guandg0929@smu.edu.cn; Jun Wang, wangjun@fosu.edu.cn; Bin Yu, yubin@smu.edu.cn

Supporting information to https://doi.org/10.26599/NR.2026.94908539

Table S1: Composition of AsCu NP batches

Component	Batch A	Batch B	Batch C	Mean ±SD
$CuCl_2$ (mg)	6	30	60	32.00 ± 27.06
As (mg)	3	15	45	21.00 ± 21.63
DSPE-PEG_{2000} (mg)	6	30	60	32.00 ± 27.06
DMF (mL)	1	3	6	3.33 ± 2.52
Distilled water (mL)	20	30	60	36.67 ± 20.82

$CuCl_2$, Copper chloride; As, Astaxanthin; DSPE-PEG, 1, 2-Distearoyl-sn-glycero-3-phosphoethanolamine-Poly(ethylene glycol); DMF, N,N-Dimethylformamide.

Table S2: The atomic concentration measured by X-ray photoelectron spectroscopy (XPS) on the surface of the nanoparticle

Name	Peak BE	Height CPS	FWHM (eV)	Area (P) CPS.eV	Area (N) TPP-2M	Atomic %
C1s	284.57	113039.81	1.56	280301.6	3929.91	78.01
Cu2p	932.39	3124.75	1.96	16246.79	15.27	0.3
N1s	399.33	3024.31	1.42	7907.47	71.43	1.42
O1s	532.17	83729.58	1.69	168646.52	978.56	19.42
P2p	133.66	1848.02	1.79	4500.55	42.57	0.84

BE, Binding Energy; CPS, counts per second; FWHM, Full Width at Half Maximum; eV, kinetic energy; TPP-2M, Tanuma, Powell, Penn 2 Method.

Table S3: Preparation of gel formulations

Sample	Physical characteristics	PBS (mL)	HPCH (mg)
Gel	White Odorless	2	40
As	Orange-red Odorless	2	40
Cu	Blue Odorless	2	40
AsCu@DSPE-PEG_{2000}	Orange Odorless	2	40

As, Astaxanthin; Cu, Ion copper; DSPE-PEG, 1, 2-Distearoyl-sn-glycero-3-phosphoethanolamine-Poly(ethylene glycol); PBS, Phosphate-buffered saline; HPCH, hydroxypropyl chitin.

Table S4: Reference primer sequences for RT-qPCR

Gene	Forward primer (5′–3′)	Reverse primer (5′–3′)
Tlr9	GCTGTCAATGGCTCTCAGTTCC	CCTGCAACTGTGGTAGCTCACT

Akt1	GGACTACTTGCACTCCGAGAAG	CATAGTGGCACCGTCCTTGATC
Mapk8	CGCCTTATGTGGTGACTCGCTA	TCCTGGAAAGAGGATTTTGTGGC
Ido1	GCAGACTGTGTCCTGGCAAACT	AGAGACGAGGAAGAAGCCCTTG
MMP9	GCTGACTACGATAAGGACGGCA	TAGTGGTGCAGGCAGAGTAGGA
Csf1r	TGGATGCCTGTGAATGGCTCTG	GTGGGTGTCATTCCAAACCTGC
Src	GTTGCTTCGGAGAGGTGTGGAT	CACCAGTTTCTCGTGCCTCAGT
iNOS	GAGACAGGGAAGTCTGAAGCAC	CCAGCAGTAGTTGCTCCTCTTC
IL-6	TACCACTTCACAAGTCGGAGGC	CTGCAAGTGCATCATCGTTGTTC
TNF-α	GGTGCCTATGTCTCAGCCTCTT	GCCATAGAACTGATGAGAGGGAG
Arg-1	CATTGGCTTGCGAGACGTAGAC	GCTGAAGGTCTCTTCCATCACC
CD206	AGCCAACACCAGCTCCTCAAGA	CAAAACGCTCGCGCATTGTCCA
IL-10	CGGGAAGACAATAACTGCACCC	CGGTTAGCAGTATGTTGTCCAGC
OCN	GCCAATGGCAAAGATGACCACAG	TGCGTGGAGTATCCATCTCTGC
OPN	GCTTGGCTTATGGACTGAGGTC	CCTTAGACTCACCGCTCTTCATG
Runx2	CCTGAACTCTGCACCAAGTCCT	TCATCTGGCTCAGATAGGAGGG
GAPDH	CATCACTGCCACCCAGAAGACTG	ATGCCAGTGAGCTTCCCGTTCAG

Table S5: Quantitative microarchitectural analysis of femoral regions of interest in a mice osteomyelitis model

	Control	Gel	As@Gel	Cu@Gel	AsCu@Gel
BMD (g/cm^3)	0.20±0.06	0.27±0.08	0.17±0.11	0.27±0.03	0.32±0.02
BV/TV (%)	21.12±4.26	31.29±5.42	22.62±7.01	30.56±2.71	34.63±2.81*
Tb.Th (mm)	0.10±0.00	0.11±0.02	0.10±0.01	0.12±0.00**	0.13±0.01
Tb.N (mm^{-1})	2.15±0.44	2.23±0.37	2.55±0.18	2.77±0.35*	2.86±0.11
Tb.Sp (mm)	0.25±0.02	0.25±0.02	0.27±0.01	0.21±0.05	0.22±0.03
SMI	2.40±0.23	2.37±0.23	2.54±0.20	2.11±0.04	2.14±0.19
BS/BV (mm^{-1})	42.97±4.33	37.88±7.97	43.17±8.51	36.79±3.23	31.92±2.19
i.S (mm^2)	0.57±0.09	0.78±0.04	0.65±0.12	0.64±0.13	0.76±0.12
Tb.Pf (mm^{-1})	17.03±2.97	14.40±2.62	15.14±2.79	15.66±2.51	12.79±1.68

BMD, bone mineral density; BV/TV, percent bone volume; Tb.Th, trabecular thickness; Tb.N, trabecular number; Tb.Sp, trabecular separation; SMI, structure model index; BS/BV, bone surface/volume ratio; i.S, intersection surface; Tb.Pf , trabecular pattern factor. Number of repetitions of all experiments n = 3.
Data are expressed as mean ± SD vs. the control group, $^*p < 0.05$ and $^{**}p < 0.01$.

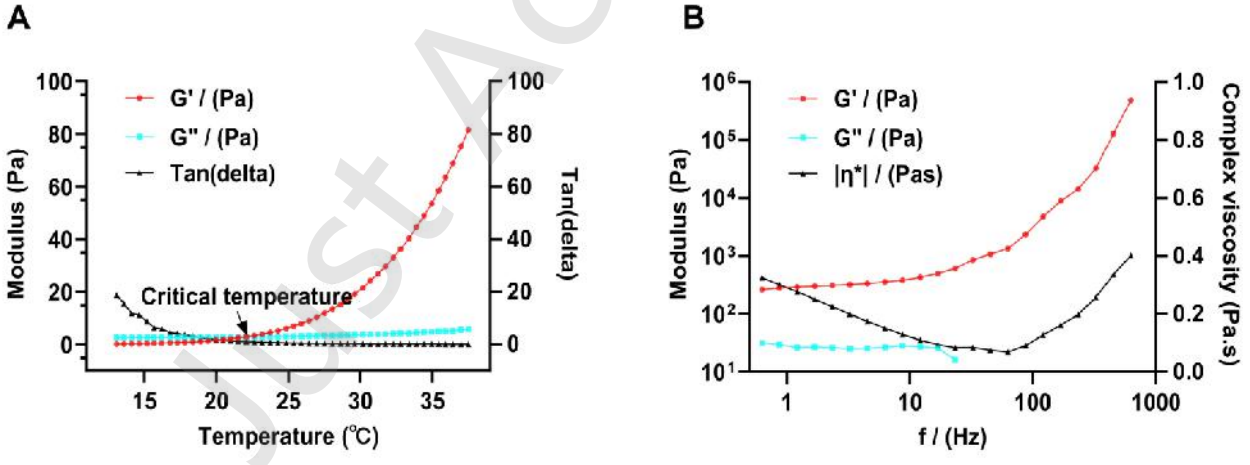

Figure S1. Rheological characterization of AsCu@Gel. (A) A temperature sweep (13-37 °C) displays the storage modulus (G′), loss modulus (G″), and loss tangent (tan). The crossover near 16-17 °C indicates the sol- gel transition, while G′ increases to greater than 80 Pa at 37 °C, confirming formation of a stable, elastic network. (B) Frequency sweep at 37 °C demonstrates solid- like behavior (G′ > G″) across 0.6-600 rad/s. The decrease in complex viscosity (η*) with increasing frequency indicates shear- thinning, which is essential for injectability. Data are expressed as mean ± SD (n = 3).

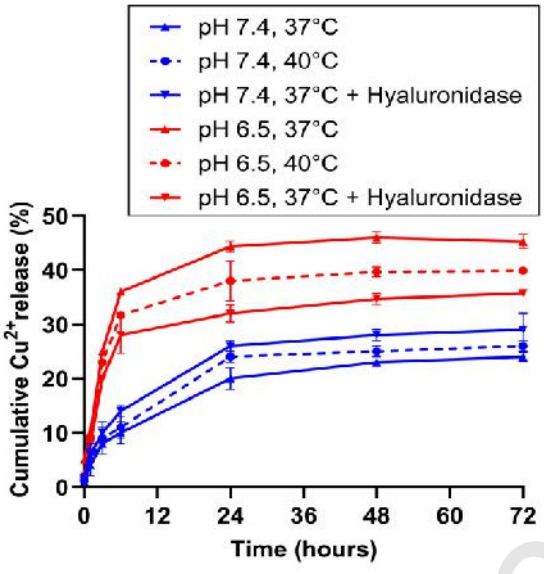

Figure S2. *In vitro* cumulative release profiles of Cu^{2+} from the AsCu@Gel composite under various simulated physiological conditions. Release was evaluated over 72 h in PBS at different pH levels (7.4 vs. 6.5), temperatures (37 °C vs. 40 °C), and with or without hyaluronidase (100 μg/mL). The results demonstrate that Cu^{2+} release is primarily increased at lower pH (6.5), while elevated temperature (40 °C) and the presence of hyaluronidase further enhance but do not surpass the pH-driven release effect. Data are expressed as mean ± SD (n = 3).

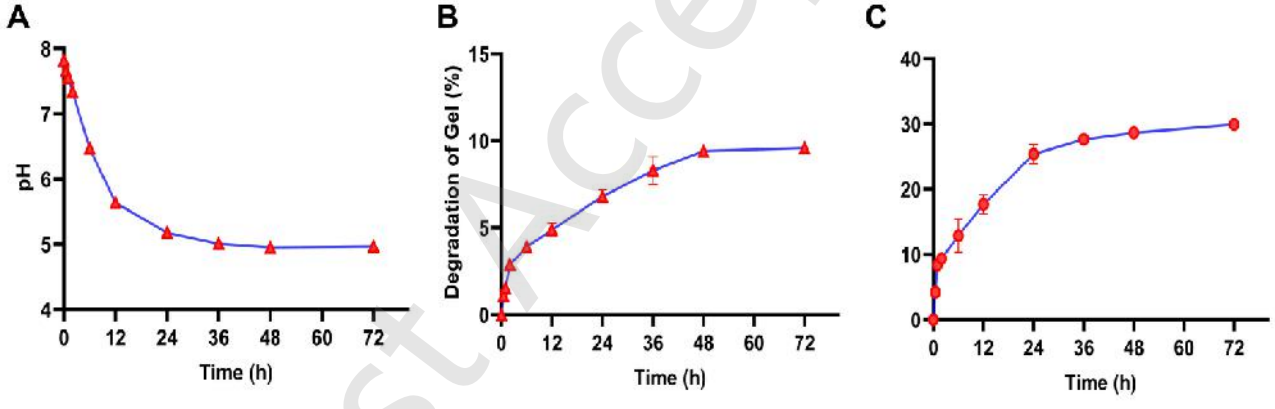

Figure S3. *In vitro* degradation kinetics and release correlation of the AsCu@Gel composite under physiological conditions (PBS, pH 7.4, 37 °C). (A) pH change of the incubation medium over 72 h. The rapid decline to an acidic plateau (pH 5.0) indicates a microenvironmental shift, likely resulting from Cu^{2+}/H^{+} exchange, which triggers pH-responsive swelling of the hydroxypropyl chitin matrix. (B) Cumulative mass loss of the hydrogel. The plateau at approximately 9.5% indicates that the crosslinked network remains largely intact (>90% mass retention), highlighting its structural stability. (C) Cumulative release of Cu^{2+} from the hydrogel. The tri-phasic profile, with an initial burst (<2 h), sustained release (2-24 h), and a final plateau (90% at 72 h), suggests a swelling and diffusion-controlled mechanism rather than bulk erosion. Data are expressed as mean ± SD (n = 3).

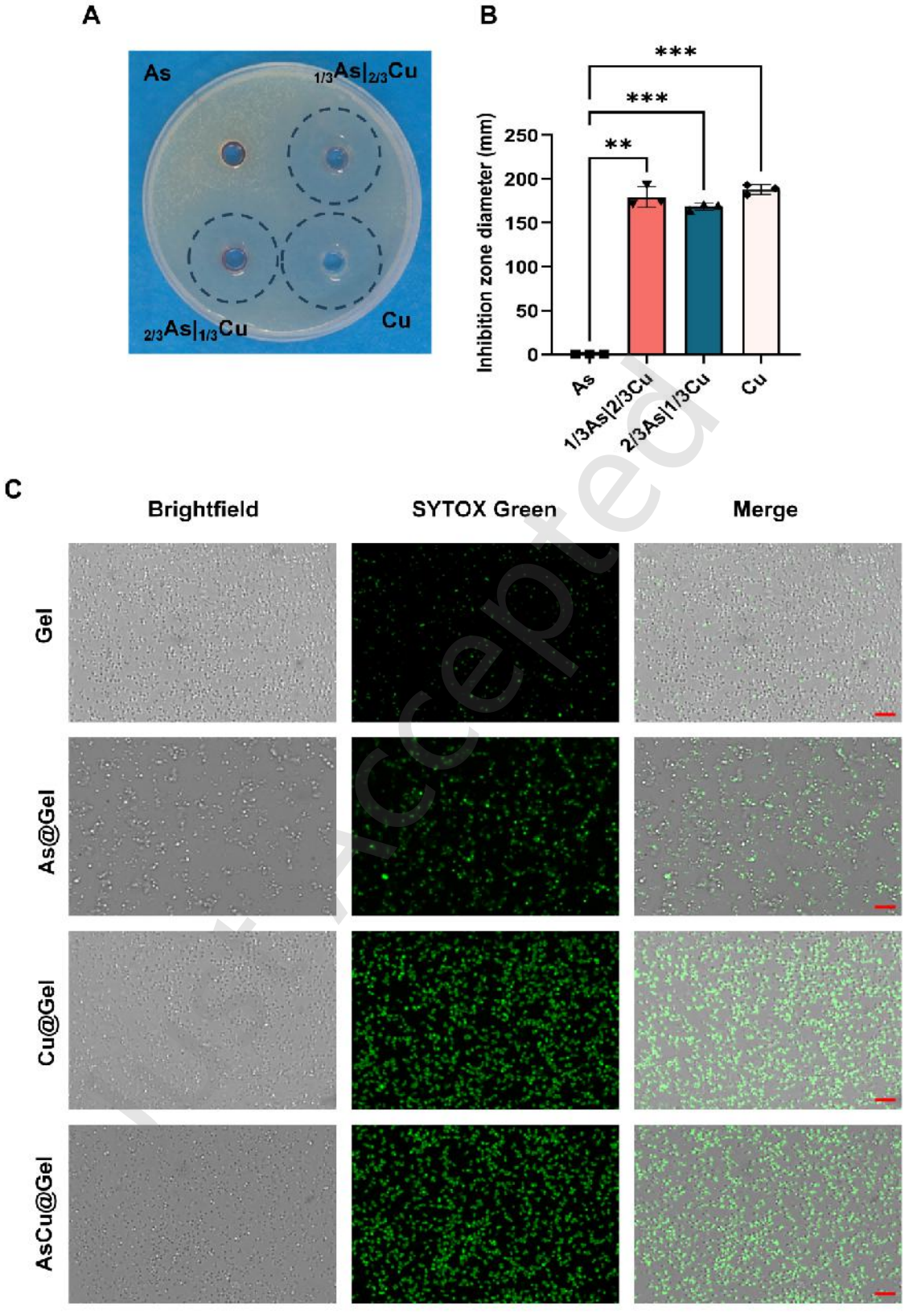

Figure S4. *In vitro* antibacterial evaluation of hydrogels. (A) Photographs of inhibition zones produced by various hydrogel discs against *S. aureus* after 24 h of incubation. Clear zones surrounding the discs indicate bacterial growth inhibition. The As-Cu composite hydrogel (AsCu@Gel) exhibits the largest inhibition zone diameter, indicating superior broad-spectrum antibacterial activity. (B) Quantitative analysis of bacterial viability following co-culture with hydrogels, determined by OD_{600} measurements. (C) Representative fluorescent microscopy images (Brightfield, SYTOX Green, and Merge). Green fluorescence (SYTOX Green) stains bacteria with compromised membranes, directly visualizing the membrane-disrupting bactericidal mechanism of the Cu and AsCu hydrogels. Data are expressed as mean ± SD (n = 3). $^{**}p < 0.01$; $^{***}p < 0.001$.

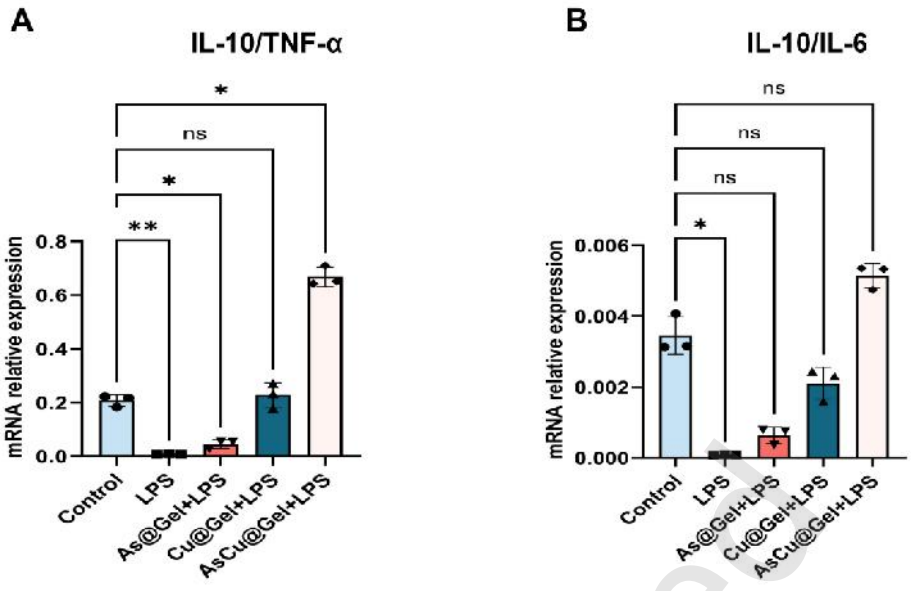

Figure S5. Expression levels of the M2/M1 ratio macrophage marker genes. (A) IL-10/TNF-α and (B) IL-10/IL-6. Data are expressed as mean ± SD (n = 3). ns = not significant; *$p < 0.05$; **$p < 0.01$.

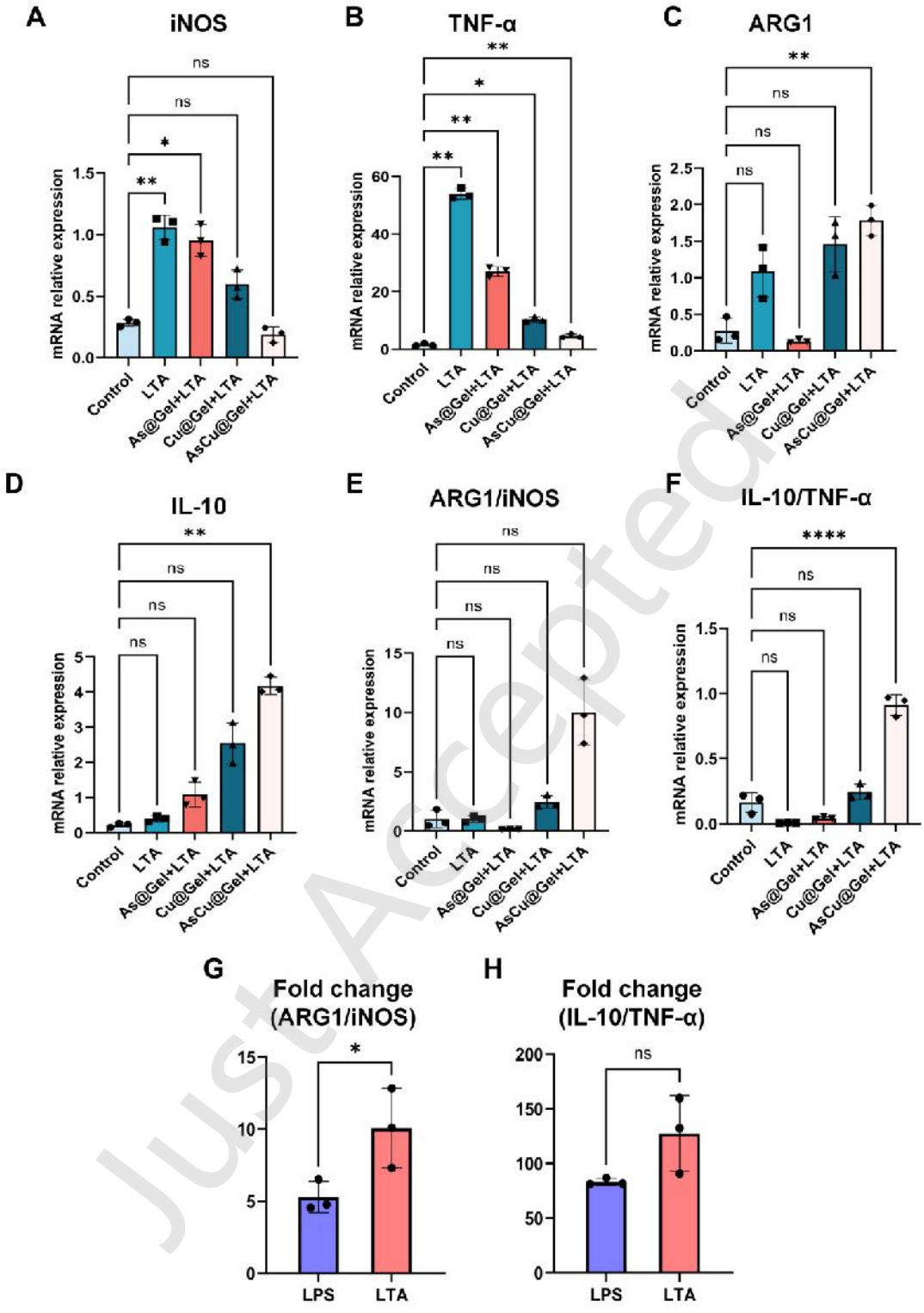

Figure S6. (A-H) AsCu@Gel demonstrates increased immunomodulatory efficacy under LTA-specific stimulation. (G) Fold change in the ARG1/iNOS ratio, an established marker of M2 polarization, following AsCu@Gel treatment compared to stimulated controls. (H) Fold change in the IL-10/TNF-α ratio, indicating the balance between anti-inflammatory and pro-inflammatory cytokines. Data are expressed as mean ± SD (n = 3). ns = not significant; *$p < 0.05$; **$p < 0.01$; ****$p < 0.0001$.

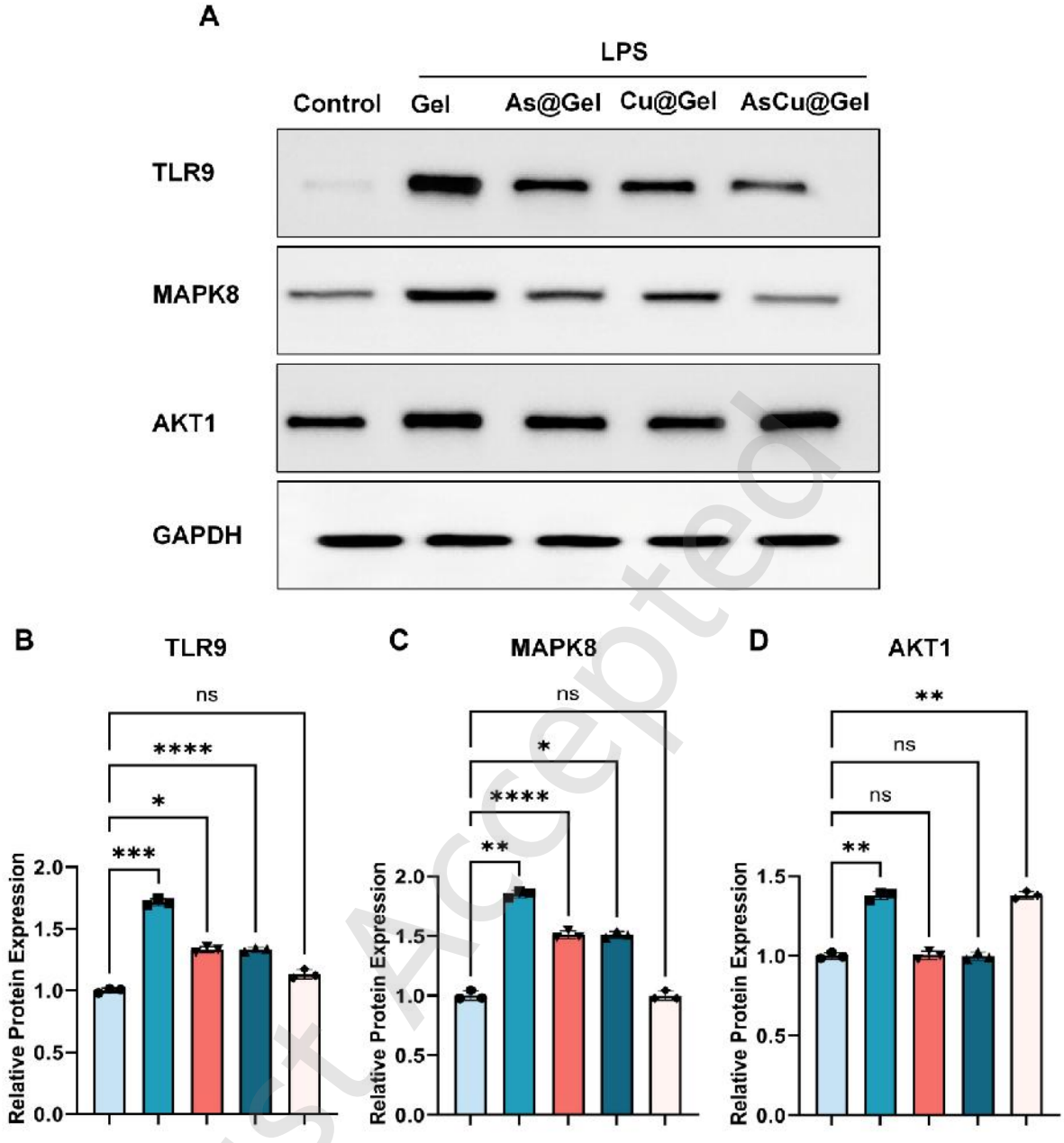

Figure S7. Protein-level validation demonstrates coordinated signaling reprogramming induced by AsCu@Gel. (A) Representative Western blots and (B–D) quantification of total TLR9, MAPK8, and AKT1 expression in RAW264.7 macrophages subjected to various treatments. AsCu@Gel treatment resulted in a significant upregulation of AKT1 compared to LPS-stimulated controls, while differentially modulating TLR9 and MAPK8 levels (B&C). Data are expressed as mean ± SD (n = 3). GAPDH was used as a loading control. ns = not significant; *$p < 0.05$, **$p < 0.01$, ***$p < 0.001$; ****$p < 0.0001$.

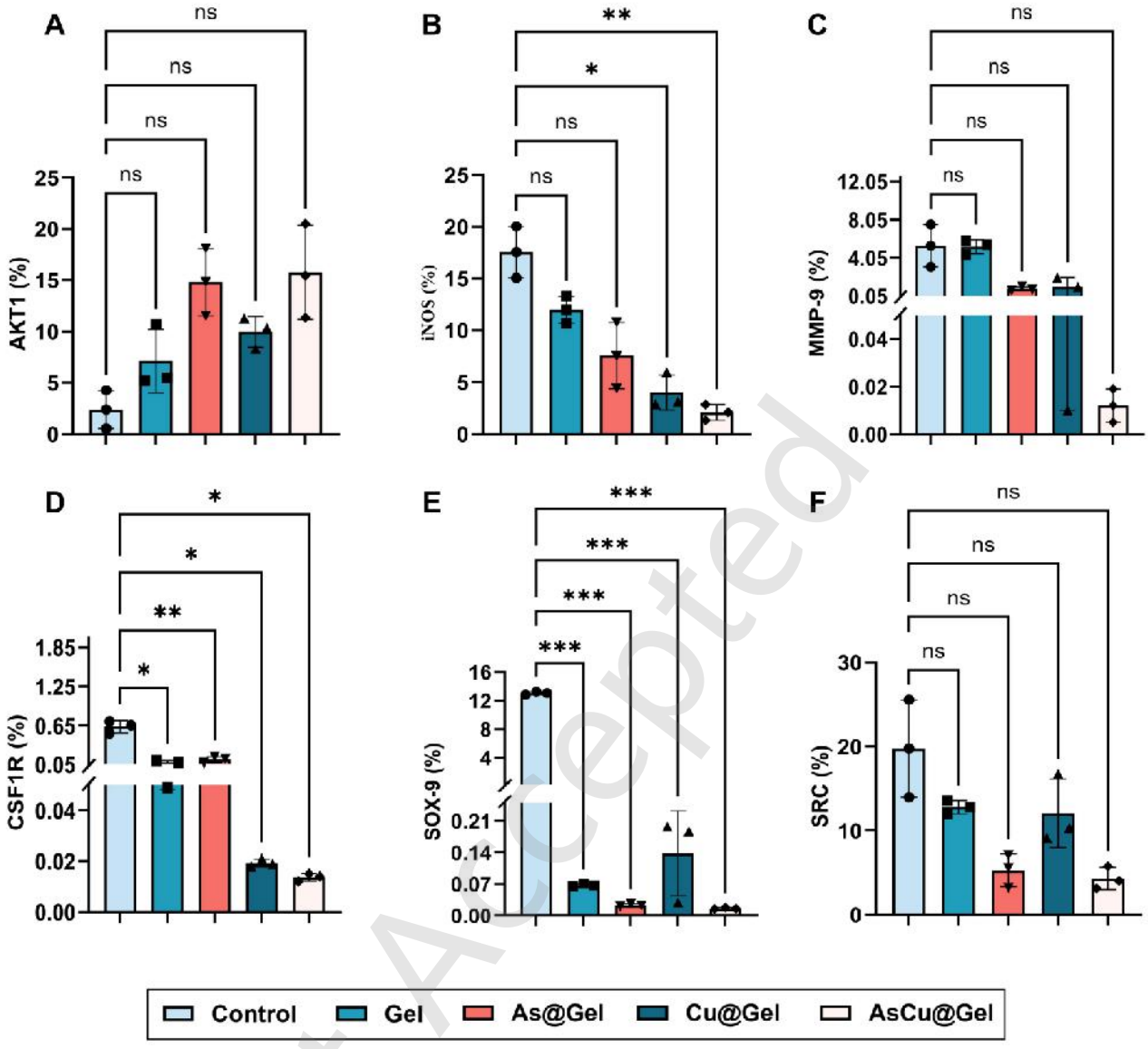

Figure S8. Immunofluorescence staining results for the markers. (A) AKT1, (B) iNOS, (C) MMP-9, (D) CSF1R, (E) SOX-9, and (F) SRC in the context of acute *Staphylococcal* osteomyelitis. Data are expressed as mean ± SD (n = 3). ns = not significant; *$p < 0.05$; **$p < 0.01$; ***$p < 0.001$.

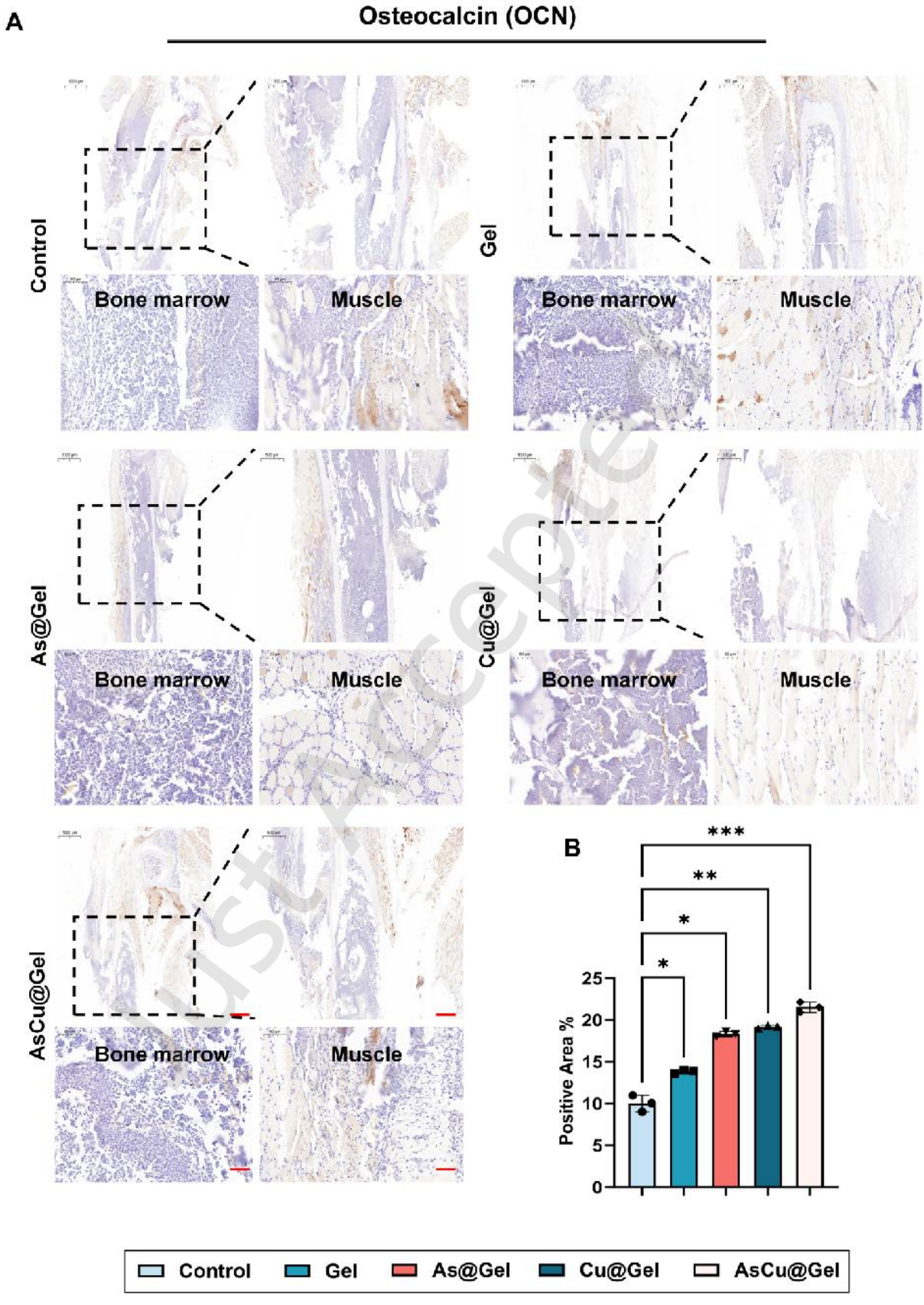

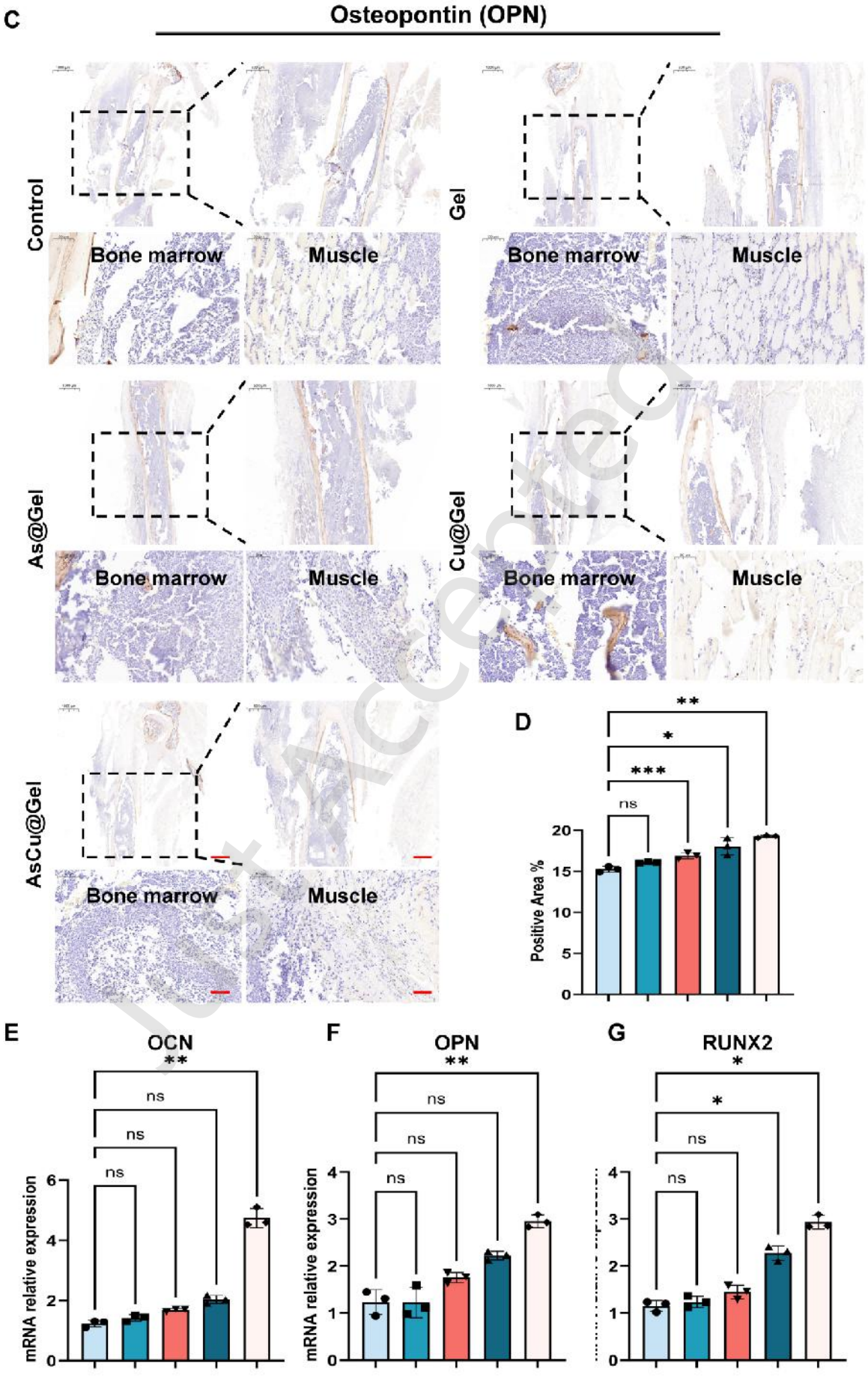

Figure S9. Osteogenic marker expression following AsCu@Gel treatment. (A) *In vivo* immunohistochemistry staining demonstrates

OCN expression and (B) quantifies the positive staining area (%) for OCN (n = 3) in bone tissue from Control, Gel, As@Gel, Cu@Gel, and AsCu@Gel groups. Scale bars: top left, 1000 μm; top right, 500 μm; bottom, 50 μm. (C) *In vivo* immunohistochemistry staining demonstrates OPN expression, and (D) quantifies the positive staining area (%) for OPN (n = 3) in bone tissue from the same groups. Scale bars: top left, 1000 μm; top right, 500 μm; bottom, 50 μm. (E-G) *In vitro* qPCR results present relative mRNA expression levels of OCN, OPN, and RUNX2, normalized to GAPDH (n = 3). Data are expressed as mean ± SD (n = 3). ns = not significant; *$p < 0.05$; **$p < 0.01$; ***$p < 0.001$.

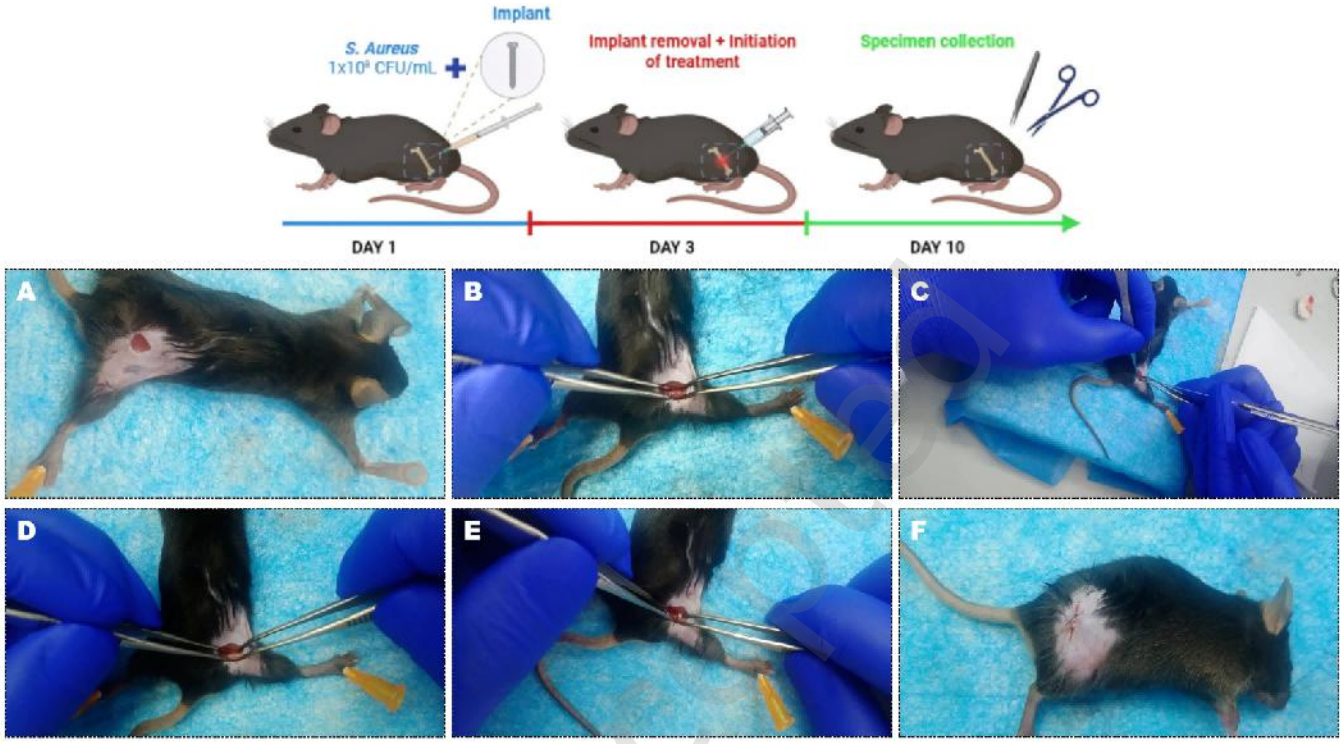

Figure S10. Surgical implantation procedure. (A) Lateral incision over the femoral midshaft. (B) Creation of a 0.5 mm defect using a 27G needle (0.36 mm outer diameter) attached to a 1 mL syringe. (C) Injection of bacterial suspension (1×10^8/CFU) into the defect via microsyringe. (D) Bacterial solution covering the defect. (E) Placement of the implant, and (F) Closure of muscle and skin layers with sutures, securing the implant in place.

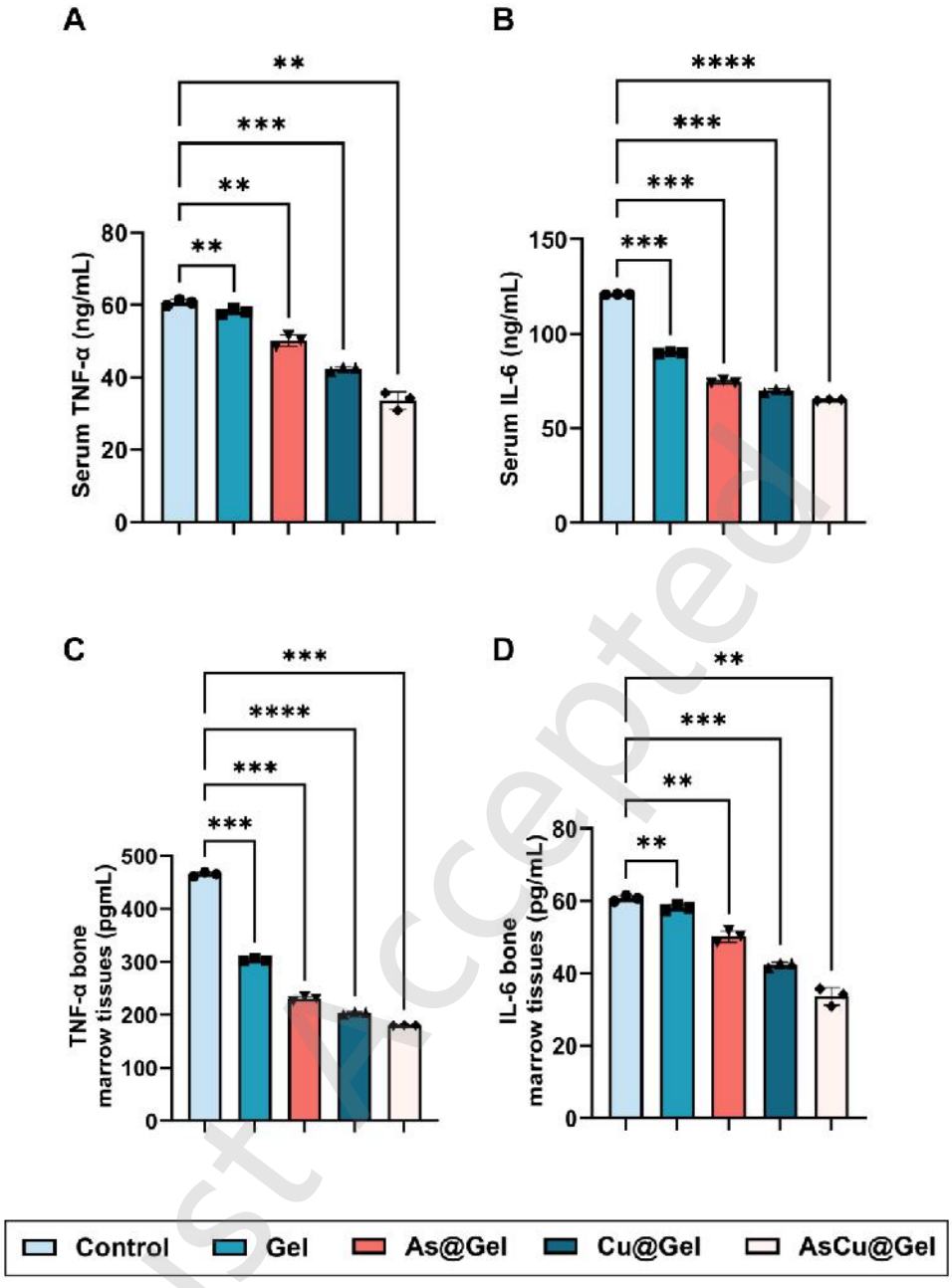

Figure S11. AsCu@Gel reduces inflammation both systemically and locally. Pro-inflammatory cytokines (A) TNF-α and (B) IL-6 were quantified in mouse serum, and (C, D) in bone marrow homogenates after 7 days of treatment. Coordinated suppression of these cytokines in both compartments demonstrates the potent systemic anti-inflammatory effect of the AsCu@Gel platform. Data are expressed as mean ± SD (n = 3). $^{**}p < 0.01$; $^{***}p < 0.001$; $^{****}p < 0.0001$.

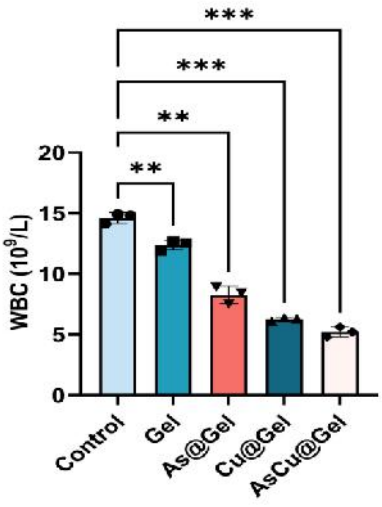

Figure S12. AsCu@Gel restores systemic immune homeostasis by resolving infection-driven leukocytosis. Peripheral white blood cell (WBC) counts were quantified after 7 days of treatment in a murine acute osteomyelitis model. Marked leukocytosis in the untreated control and gel-only groups indicates severe systemic infection. AsCu@Gel treatment effectively controlled the immune response, reducing WBC counts to near-normal levels and demonstrating superior resolution of infection and associated systemic effects. Data are expressed as mean ± SD (n = 3). $^{**}p < 0.01$; $^{***}p < 0.001$.

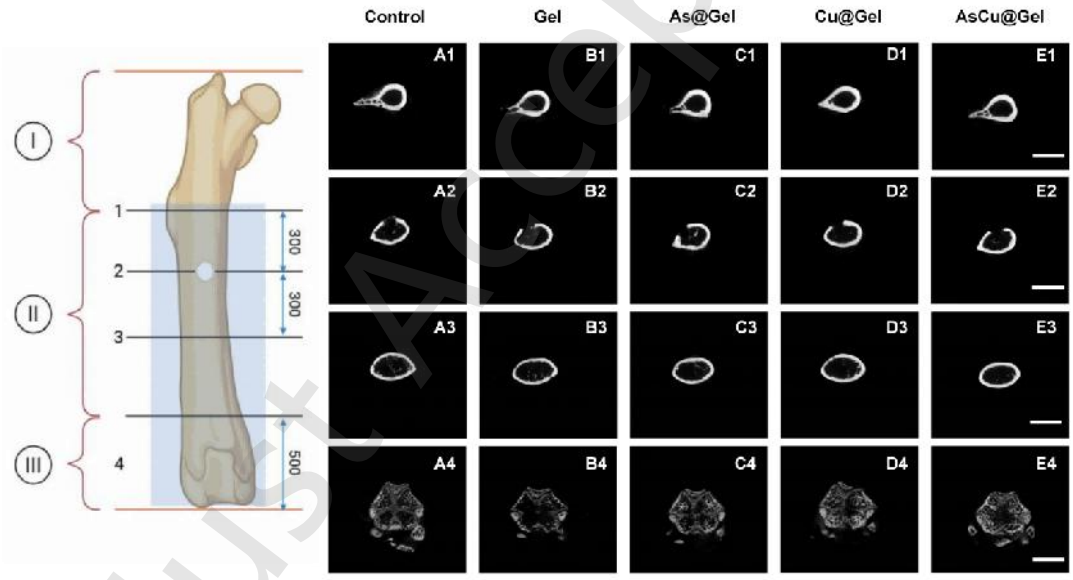

Figure S13. Schematic of X-ray microscopic 2D imaging of murine femurs, showing section locations and cortical bone cross-sections across groups. I: Proximal femur (1. cortical window shifted 300 slices up). II: Midshaft (central 1/3 femoral length; cortical window ±300 slices down). III: Distal femur (trochlear groove apex to posterior condyles). A1-A3/B1-B3/C1-C3/D1-D3/E1-E3: Cortical bone (Scale bars: 1 mm); A4/B4/C4/D4/E4: Condylar trabecular bone (Scale bars: 2 mm).

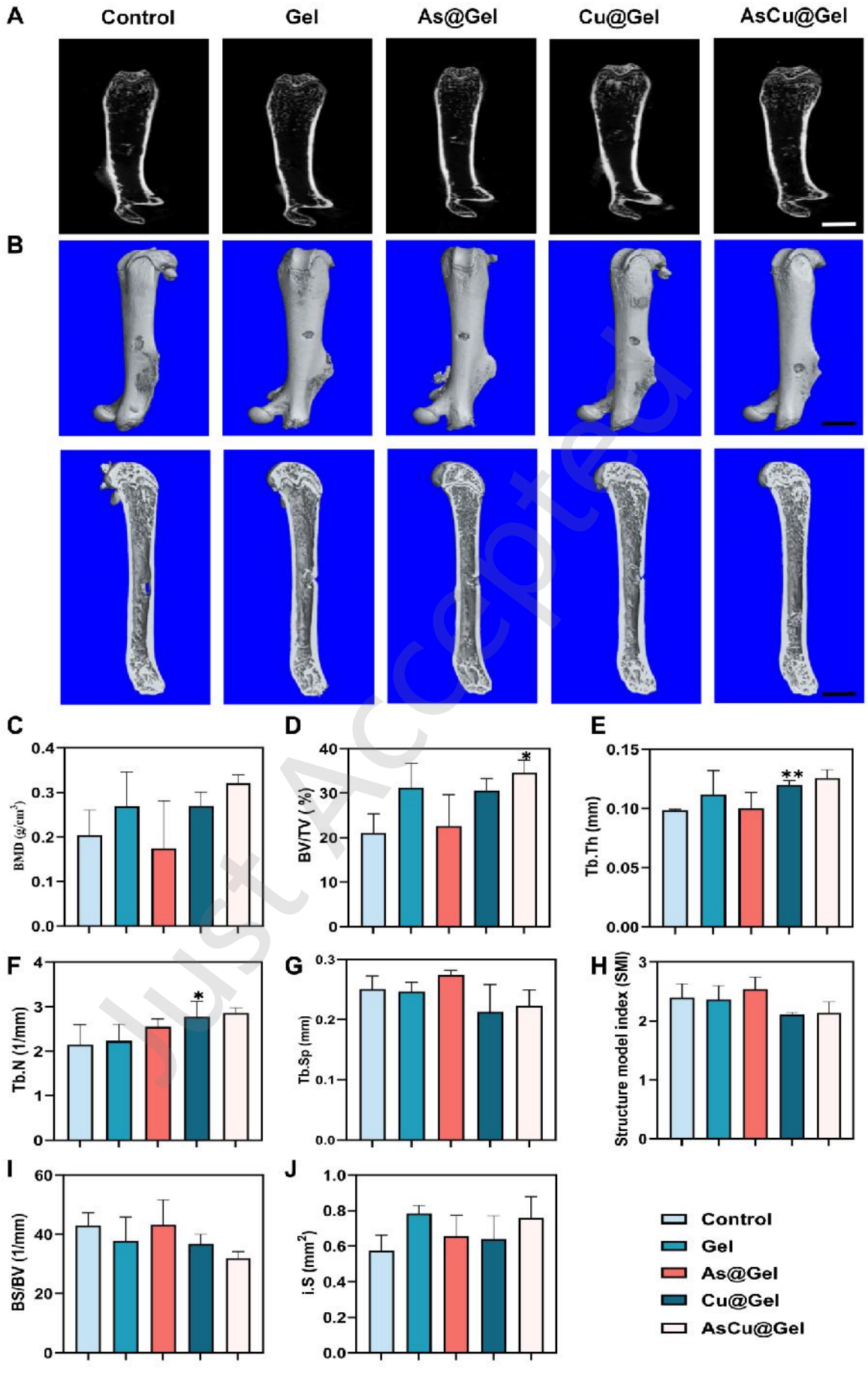

Figure S14. (A) X-ray images illustrating the osteomyelitis group alongside the Gel, Cu@Gel, As@Gel, and AsCu@Gel groups. (B) Three-dimensional reconstructions of the osteomyelitis group and the Gel, Cu@Gel, As@Gel, and AsCu@Gel groups, including their

respective cross-sections. Quantitative analysis of the entire femur, detailing parameters such as (C) bone mineral density (BMD), (D) bone volume fraction (BV/TV), (E) trabecular thickness (Tb.Th), (F) trabecular thickness (Tb.N), (G) trabecular separation (Tb.Sp), (H) structure model index (SMI), (I) bone surface/volume ratio (BS/BV), and (J) intersection surface (i.S) for the osteomyelitis group in comparison to the Gel, Cu@Gel, As@Gel, and AsCu@Gel groups. (Scale bars: 2 mm). Data are expressed as mean ± SD (n ≥ 3). *$p < 0.05$; **$p < 0.01$.

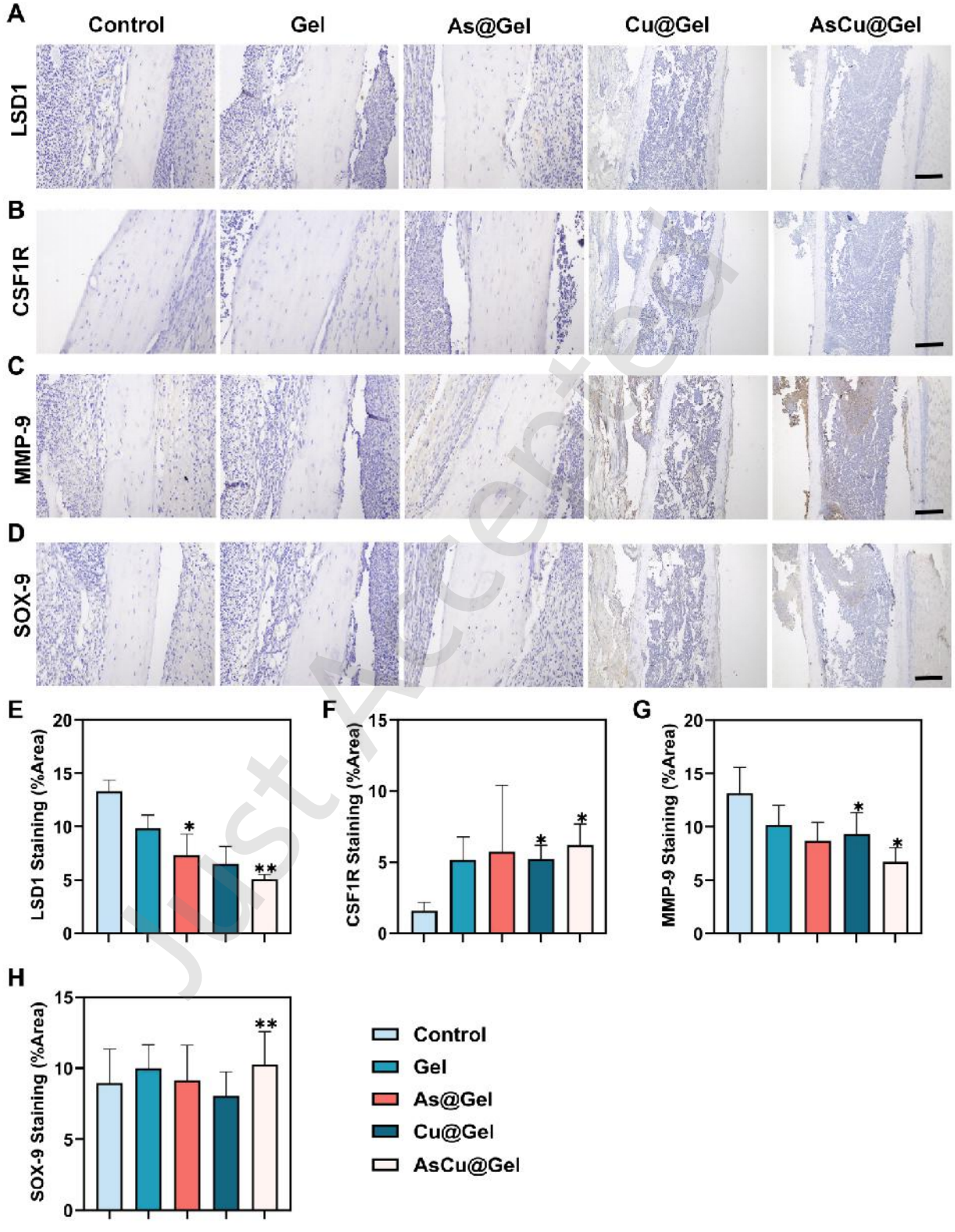

Figure S15. Modulation of macrophage polarization markers by hydrogel treatments in decalcified femur slices at day 10 post-surgery. (A) LSD1 (M1 marker) immunohistochemical staining. AsCu@Gel shows significant reduction vs. Control. (B) CSF1R (M2 marker) expression. (C) MMP-9 (M1 marker) suppression across treatments. AsCu@Gel reduces expression vs. Control. (D) SOX-9 (M2 marker) upregulation in AsCu@Gel. (E-H) Quantitative analysis of (E) LSD1, (F) CSF1R, (G) MMP-9, and (H) SOX-9 expression. (Scale bars: 100 μm). Data are expressed as mean ± SD (n ≥ 3). *$p < 0.05$; **$p < 0.01$.